UNIVERSITY OF OKLAHOMA

GRADUATE COLLEGE

EFFECTS OF FLOW RATE ON MESENCHYMAL STEM CELL OXYGEN CONSUMPTION RATES IN 3D BONE TISSUE ENGINEERED CONSTRUCTS CULTURED IN PERFUSION BIOREACTOR SYSTEMS

A THESIS

SUBMITTED TO THE GRADUATE FACULTY

in partial fulfillment of the requirements for the

Degree of

MASTER OF SCIENCE

By

MICHAEL LARUE FELDER
Norman, Oklahoma
2019

EFFECTS OF FLOW RATE ON MESENCHYMAL STEM CELL OXYGEN CONSUMPTION RATES IN 3D BONE TISSUE ENGINEERED CONSTRUCTS CULTURED IN PERFUSION BIOREACTOR SYSTEMS

A THESIS APPROVED FOR THE
STEPHENSON SCHOOL OF BIOMEDICAL ENGINEERING

BY

Dr. Vassilios I. Sikavitsas, Chair

Dr. Roger G. Harrison

Dr. Edgar A. O'Rear III

Acknowledgements

I would first like to thank my advisor, Dr. Vassilios Sikavitsas, for all his help and guidance throughout my time here at OU. He was always able to point me in the right direction when I had questions, and ensured I had a good understanding of the work I was doing. Needless to say, I would not be at this point in my degree without his support. I'd also like to thank the other two members of my committee, Dr. Edgar O'Rear and Dr. Roger Harrison. Each of them were eager to help me, both in providing feedback on my research and in the classes I took with them. Additionally, I'd like to thank Dr. Matthias Nollert and Dr. Robert Shambaugh for their assistance inside and outside the lab. Dr. Shambaugh was a great help in providing me some of the materials I needed to complete my research. Furthermore, Dr. Nollert gave me excellent advice about graduate school, and life in general, helping me keep my head above water when things were tough. All of these professors played an integral role in the engineer I am today.

I would also like to thank the CBME and SBME departments for everything they've done to help me throughout my academic career at OU. The faculty and staff in these departments were genuinely invested in me, and always did everything they could to help me succeed. I would like to specifically thank Terri Colliver and Shayla Glover, for the countless questions they happily answered over the years.

I would also like to thank the other graduate students in CBME and SBME. Thank you to Sabrina Garner, MJ James, Alexis Woodward, Ben Southard, Daniel Karami, Caroline Bantug, James Buerck, Gabriela Faria, and Patrick McKernan. I appreciate all your friendships, and could not have done this without your support. I would also like to thank Aaron Simmons for continuing to answer my questions about lab, even though he graduated three years ago and was probably tired of hearing about oxygen sensors.

Lastly, I'd like to say thank you to my family. Victoria and Amanda, thank you for being fantastic sisters who always listened when I had problems and were there to celebrate when I had slightly fewer problems. And to my parents, thank you for everything. I am so fortunate to have the best mom and dad to guide and support me in all that I do.

Table of Contents

List of Tables

List of Figures

Abstract

Bone grafts comprise a multibillion dollar industry, with over a million grafts occurring each year around the world. These grafts are commonly autologous or allogenic. Autologous grafts are taken from the patient, and are sourced from a donor site from the patient's body. Allogenic grafts are derived from a cadaver donor. Each of these graft types are associated with issues such as donor site morbidity in autologous grafts and immunological response in allogenic grafts. Bone tissue engineered constructs are a logical approach to combat the issues commonly encountered with current autologous and allogenic bone grafting techniques. While it is possible to grow bone tissue engineered constructs *in vitro,* it is necessary to destroy the construct to determine the number and type of cells present. Recent work has led to the development of models that have the potential to predict the number and types of cells within the construct through metabolite monitoring. The metabolites, such as glucose and oxygen, are used to monitor cell growth while the construct remains in the bioreactor, eliminating the need to lyse cells and destroy the scaffold. This allows for the development of quality assurance methodologies that are explicitly utilized on the specific graft to be used on a patient. These models, however, neglect to account for factors affecting the construct, such as flow rate and scaffold geometry. This study aimed to determine the flow characteristics present within the bioreactor system, and hoped to quantify the effects of these characteristics on oxygen uptake rates of mesenchymal stem cells. The work done utilized a residence time distribution analysis using an easily monitored dye to develop residence time distribution functions, and associated these functions with literature values to characterize the flow patterns and residence times of media moving through the construct. Findings indicate that flow within the bioreactor system is well approximated by linear tubular flow reactors, associated with gradients in the radial

direction at low flow rates. Additionally, oxygen uptake rates of stem cells in these conditions have a strong linear correlation with residence times of media in the cassette, providing the data needed to develop a predictive model for oxygen uptake rates. These models also show promise for providing corrective functions for on-line oxygen monitoring systems in current bioreactor designs.

1. Introduction

1.1 Relevance and Current Market

Bone damage due to trauma or disease is prevalent worldwide. In many instances, a bone graft is required to treat such damage. A bone graft is the term referring to an intricate matrix of transplanted bone, or bone substitute that aids in the repair or replacement of a damaged bone. Over 500,000 patients receive bone grafts annually in the United States and Europe, and 430,000 incidents worldwide involve autologous bone [1, 2]. The total cost of bone grafts in the United States and Europe was estimated to be $3 billion in 2012, and is only expected to increase in the coming years [1]. This rising demand for bone grafts provides a prime market for a viable alternative to current standards in orthopedics and dentistry.

1.2 Bone Graft Characterization

Current solutions for bone defects typically center on the use of various graft types including autologous grafts, allogenic grafts, and xenografts [3-6]. These bone grafts differ in where they are sourced. Autologous bone grafts are taken from a separate location on the patient's body, oftentimes the iliac crest [2, 7]. Allogenic grafts are sourced from a cadaver [4, 5, 8]. Xenografts are bone grafts taken from another species, and prepared to serve as a calcified matrix [4]. Each of these grafts has benefits and downsides. Autologous grafts rarely suffer from immunological response, as they are sourced from the patient's own body, and maintain good osteogenic, osteoconductive, and osteoinductive properties [5, 7, 9]. However, donor site morbidity, pain, and infection have high incidence rates, even with current surgical techniques [2, 7, 9, 10]. Additionally, autologous grafts have limited availability, and can lead to additional complications such as fat embolisms and deep vein thrombosis [11, 12]. Allogenic grafts have

higher availability, in addition to maintaining osteoconductive and some osteoinductive characteristics [4]. These grafts also show comparable results to autografts when treated with osteogenic factors, such as bone morphogenetic proteins [8]. Furthermore, allografts are the main source of grafts for large bone defects [13]. Still, these grafts suffer from issues revolving around immunological response, mechanical properties from sterilization techniques, and high variability due to source [4, 9]. Lastly, xenografts have been shown to give promising results in dentistry, but have been shown to result in foreign body reactions and infection in orthopaedic applications, even though they are biocompatible [4, 14]. With each of these graft types, defect size plays a large role in determining the success of the graft [15]. Union rates are high for autologous grafts when compared to allogenic, especially when utilizing vascularized autologous grafts [6, 16]. Allogenic also have poor long-term outcomes, and often result in fracture and bone density loss [13]. However, allogenic grafts are often required for many arthroplasty revisions, as autogenic sources have been depleted [12, 13]. These revisions have good short-term outcomes, but long-term outcomes are highly variable [13].

Tissue engineered grafts aim to serve as an alternative to previous graft types mentioned, as they have the potential to maintain good osteogenic, osteoconductive, and osteoinductive characteristics. Furthermore, the size and morphology of the tissue engineered graft has the ability to be modified for a particular patient. Synthetic bone grafts have been used more recently. Early trials involving hydroxyapatite ceramics as alternatives for autologous grafts yielded promising results [17]. From there, work has been completed on the use of various osteoconductive polymeric or ceramic scaffolds infused with osteoinductive growth factors and pre-osteoblastic cells [3, 6]. These tissue-engineered grafts, though they show initial results consistent with autologous grafts, are not currently the go-to option for bone grafts [18, 19].

However, these recent results do show that they could potentially reach a point where they outperform autologous grafts [18].

1.3 Tissue Engineering Approach

Tissue engineering was originally described over 30 years ago as a combination of engineering and life sciences [20]. This approach has developed dramatically since then, and is now the basis for over 100 companies generating over $3.5 billion in sales each year [21]. The overarching goal of tissue engineering is to provide an alternative means of tissue replacement throughout the human body. It centers on three main criteria: biodegradable scaffolds, patient derived cells grown on these scaffolds, and chemical signals provided to cells to allow for differentiation into necessary cell types [20].

1.4 Challenges Facing Tissue Engineered Bone Grafts

Current challenges in tissue engineering focus on finding reproducible means to create tissue engineered constructs that are viable for transplants into humans. Existing methodologies require the destruction of constructs to determine their characteristics such as cellularity, development of extracellular matrices, and cell type. Due to this, FDA approval is hindered by the absence of appropriate predictive models that need to be developed. While many solutions exist to determine similar characteristics in 2D systems, 3D systems lack predictive models to accurately and consistently describe the important factors that will ultimately allow us to bring tissue engineered bone constructs to a large-scale production. This is especially true when 3D cell/scaffold constructs are cultured in flow perfusion bioreactors.

Furthermore, nutrient transfer to interiors of bone constructs is a hurdle that has yet to be completely addressed [22, 23]. Vascularization of bone grafts is a barrier due to the fact that scaffold design is insufficient to promote architecture that mimics native tissue in its entirety [23, 24]. Even more, complete control of nutrients to cells, specifically oxygen, is vital to ensure that cells behave in a manner that is consistent with native tissue [23]. However, current bioreactor designs neglect to take this into consideration. Static cultures of 3D cell/scaffold constructs remain heavily utilized although they generate often the most severe nutrient limitations to cells residing deep inside these scaffolds.

1.5 Characterization of Natural Bone Tissue

3D tissue engineered bone constructs need to maintain certain physiological aspects to be consistent with natural bone present in body. As such, it is important to have a thorough knowledgebase of what constitutes bone. Bone is a living tissue, containing an organic structure of approximately 95% Type I collagen strengthened with calcium salts [25]. Within this structure live four types of bone cells: osteoblasts, osteoclasts, osteocytes, and bone lining cells [25, 26]. Each of these cells completes a different task within the bone, allowing for continued upkeep and remodeling of bones within the body [26]. Two types of bone are present in the body: cortical and cancellous [25, 27]. The physiological differences between these two types allows for heightened function of skeletal bone throughout the body, where cortical is compact and provides mechanical and protective roles while cancellous bone is the primary site for metabolic functions [25].

1.6 Cell Types and Functions

The variety of cells present in bones have progenitor cells such as mesenchymal stem cells and hematopoietic cells residing in the bone marrow. Mature and differentiated cells inhabit the bone, itself, or leave the bone entirely through the blood stream [28]. Bone modeling and remodeling are completed primarily through two cell types: osteoblasts and osteoclasts; however, bone lining cells and osteocytes also play large roles in the development and maintenance of bone structure [29, 30]. Each of these cell types interact with each other through the secretion of factors including, but not limited to, proteins, cytokines, hormones, and extracellular matrices [31-34]. It is with these factors that cells are recruited to particular locations within the bone, and bone remodeling takes place in basic multicellular units on the surface of the bone [31, 33]. These factors also induce differentiation in progenitor cells, as bone remodeling relies on a specific balance of each cell type in the basic multicellular unit [30, 33]. Mesenchymal stem cells are the progenitor cells for the osteoblastic lineage, whereas hematopoietic stem cells are the progenitor cells for osteoclasts [29]. Osteoclasts' primary function is to reabsorb the bone matrix in response to local defects [26]. The osteoblastic lineage is composed of osteoblasts, and the two terminally differentiated cell lines osteocytes and bone lining cells [30]. The primary purpose of osteoblasts is to secrete extracellular matrix to build up the bone, while osteocytes and bone lining cells help control the level of remodeling occurring in a particular area of bone [29, 30]. Osteocytes are cells buried within the bone matrix, and provide signaling to the other cell types depending on a variety of factors including mechanical loading [35]. Bone lining cells are found on the surface of bone, and aid in cell recruitment in response to mechanical stress, and have been found to return to an osteoblastic state in response to mechanical stimuli [30, 36].

Furthermore, bone lining cells serve a vital role in controlling osteoclast activity and the formation of the basic multicellular unit [26].

Mesenchymal stem cells clearly play a large role in the development and maintenance of bone in the body, as they are the progenitor cells for osteoblasts, osteocytes, and bone lining cells [29]. These cells were originally identified in the mid-20th century, but were not recognized as playing a role in regeneration of tissue until more recently. Early research on mesenchymal stem cells revealed their highly proliferative properties, and showed they could be properly controlled to differentiate into different lineages *in vitro* [37]. Other research identified their potential to be used in regenerative medicine, as they were able to be extracted, differentiated, and re-implanted into the body and perform the activities of that cell *in vivo* [38]. Since then, work has been completed, and mesenchymal stem cells are much more well-characterized. To be considered a mesenchymal stem cell, certain criteria must be met. Originally outlined by The International Society for Cellular Therapy, these cells must be adherent to plastic, differentiate in to chondrocytes, osteoblasts, and adipocytes, and express certain surface markers to be considered mesenchymal stem cells [39, 40]. The large diversity in functions of mesenchymal stem cells has been increasingly researched, and now it is seen that these cells even play roles in immunological responses speed of healing [41, 42].

1.7 Physical Characterization of Bone Matrix

Two types of bone are found in the body, cortical and cancellous, and each of these types maintains different physical characteristics. Cortical bone is highly organized and contains packed collagen fibrils in the form of lamellae [25]. These lamellae run perpendicular to each other, and help form much of the structural support [25]. Cancellous bone is much more porous,

with no regular matrix [25]. Each of these bone types maintain comparable mineralization. Bone in the body is composed of approximately 50 to 70% mineral, 20 to 40% organic matrix, and 5 to 10% water [27]. Of the minerals present, the major one is calcium and phosphate in the form of hydroxyapatite [25, 27]. Other minerals include carbonate, magnesium, and acid phosphate [27]. The organic portion of the bone is a majority collagen, and helps give the bone elasticity and flexibility [27, 43]. In understanding the native bone morphology, proper scaffolds, cell types, and chemical cues can be selected to ensure a final tissue engineered bone construct will reflect the natural tissue it aims to replace.

1.8 3D Bioreactor Systems

Many different types of 3D bioreactor systems exist, such as spinner flask, rotating flask, and flow perfusion systems [44]. Each of these systems provides particular properties relating to shear stresses experienced by constructs and mass transfer of nutrients to cells. Flow perfusion bioreactors function by flowing nutrient and oxygen rich media through the construct, promoting cell migration to the center of constructs and providing controlled mechanical stimulation [44, 45]. The system is arranged by placing a scaffold seeded with cells within a cassette. This cassette serves as a means of holding the tissue engineered construct in place as media perfuses through it. Media is circulated through the system, with most contained in a reservoir outside the bioreactor setup [46]. A media inlet and outlet are positioned on the top and bottom of the scaffold, and media is perfused through the mesh scaffold seeded with cells [46]. Flow perfusion systems correct for common issues encountered in both spinner flask and rotating flask bioreactors, like the development of a fibrous layer surrounding the construct or absence of cell proliferation [46, 47]. Flow perfusion systems manage to mitigate these negative attributes while

also providing increased control over physical characteristics like shear stresses and mass transfer of nutrients to the cells, and function best for bone differentiation experiments [45, 48].

1.9 Factors in 3D Bioreactor Systems

A variety of considerations must be made when designing flow perfusion systems. In these system types, flow characteristics, scaffold architecture, and presence of cells and extracellular matrices can have large effects on the local mass transfer properties and mechanical stimulation experienced by the cells in the reactor.

1.9.1 Effects of Flow in Perfusion Bioreactors

Flow perfusion bioreactors have been selected for bone tissue engineering applications for two primary reasons centering on mass transfer and mechanical stimulation. In early bioreactor designs, mass transfer to the center of 3D scaffolds was completed primarily through diffusion; however, flow perfusion flows media directly through the interconnected pores of a scaffold, mitigating most mass transport limitations [49-51]. Furthermore, the direct control of this mass transport phenomena alone was found to have a direct effect on cell behavior in larger tissue engineered constructs [52, 53]. Flow perfusion also provides mechanical stimulation in the form of shear stress. Shear stress has been shown to have a positive effect on the differentiation of mesenchymal stem cells into osteoblasts [49, 52, 54, 55]. Even more, increased shear stress is directly proportional to the deposition of mineralized matrices [51, 56]. However, while the mass transport and shear stress environments produced by fluid flow showed direct effects on the cells' behavior, these two aspects have been shown to be highly dependent on the scaffold geometries used in each application [57].

1.9.2 Effects of Scaffold Architecture

As flow characteristics vary greatly with scaffold geometry, it is important to have knowledge of how each scaffold will behave in a given tissue engineering application [57]. Scaffolds also play a large role in cell behavior and construct success due to their surface characterization, overall geometry, and material characteristics [58-60]. In an overarching sense, material choice will be one of the primary indicators of how well a scaffold will perform. Materials will change based on the specific application, and these materials need to have clearly described mechanical properties, degradation rates, and biological activity [61]. Material choice is especially important when considering the necessity of having a modifiable scaffold that is tailored to a particular patient [60]. Scaffold architecture has a significant effect on construct success, as porosity, pore size, and overall geometry will strongly dictate the flow characteristics and microenvironments experienced by cells in a flow perfusion system [61]. Rapid prototyping is a potential solution to these issues, but the current state of manufacturing technologies is unable to consistently produce scaffolds with these porosity and pore size requirements in materials that are biologically relevant [60].

1.9.3 Summary of Effects

Both of these bioreactor characteristics, flow rate and scaffold type, are greatly related as they each have drastic effects on determining cell fate and the development of an extracellular matrix. Flow is a contributing factor to shear stress and mass transfer properties experienced by cells in a tissue engineered construct. Scaffold characteristics such as pore size and porosity also have an effect on both shear stress and mass transfer, in addition to dictating the microenvironments experienced by cells. Additionally, scaffold choice will involve aspects such

as material and geometry, both of which are highly associated with manufacturing technique. In all, it is important to have extremely characterized systems to maintain consistent predictive measures for a tissue engineered construct.

1.10 Monitoring Techniques for Tissue Engineering Bioreactors

Recently, monitoring techniques for these constructs have been developed allowing for continuous data to be collected. As such, on-line measurements hope to bypass the destructive means by which constructs are currently evaluated.

1.10.1 Oxygen Sensing

Oxygen has long been seen as a potential indicator for metabolic activity, cell proliferation, and cell culture success. Various designs for measured oxygen uptake rate have been developed for both 2D and 3D systems, with implications ranging from cellular biomass monitoring to 3D tissue engineered constructs [62-68]. 2D culture systems quantify diffusion of oxygen into media and compare these values to oxygen readings at or below the cells present in the culture [69, 70]. These monitoring techniques utilize a fluorescent dye in a material that is read with a fiber optic probe or fluorescent microscope, with the latter system using oxygen beads to map local oxygen gradients across a plate [69, 70]. Most 3D perfusion systems use a similar fluorescent dye material to monitor oxygen entering and exiting the construct, but alternative systems where electrodes are used have proven successful at high cell densities [64-68, 71]. Flow perfusion systems that measure oxygen uptake have been shown to give linear relationships with metabolic activity and cell proliferation in a 3D construct, allowing for a non-destructive means to monitor cells *in vitro* [63, 64, 68]. Differentiating cells have been shown to

change metabolic pathways, thereby changing oxygen uptake rates, but oxygen monitoring in conjunction with other on-line monitoring systems has been shown to account for these changes and predict the time-point where differentiation takes place [65].

1.10.2 Glucose Sensing

A variety of methods for measuring glucose concentrations in solutions have been developed. Each of these systems provides a potential option to monitor tissue engineered constructs continuously on-line. Amperometric sensors that are rhodinized carbon based have been developed to determine the concentration of glucose in a continuous manner [72, 73]. These sensors utilize an enzymatic reaction between glucose and glucose oxidase, and show high selectivity for glucose in medium solutions [72]. Other sensors used also center on the exploitation of glucose oxidase, however these are in direct contact with an oxygen sensitive material and a fiber-optic probe [74]. This design provides continuous measurements for at least 24 hours, in addition to maintaining high selectivity even in the presence of oxygen and other metabolites in the system [74]. Generally speaking, glucose oxidase is a vital component when determining glucose concentration in bioreactor systems.

Work completed by Simmons et al. and Meuwly et al. showed promising results for glucose to serve as an indicator of cellularity and differentiation [65, 75]. Glucose has been shown to reliably monitor proliferation in cell dense systems, in addition to serving as a dependable control for controlling cell behavior like productivity [75]. Furthermore, glucose can be used in conjunction with other monitoring systems, such as oxygen, to aid in determining both cellularity and progress of differentiation [65].

1.10.3 Resazurin Based Assays (AlamarBlue™ and Presto Blue™)

Resazurin has long time been a common indicator of cytotoxicity and cell viability [76-78]. Originally used in static 2D systems, high linearity and sensitivity have been seen, but recently work has been done to determine the potential of resazurin based assays to function in 3D bioreactor systems [76, 77, 79-81]. These assays are correlated with metabolic activity of the cells, and mainly focused on determining relationships with metabolic activity and cellularity readings in 3D perfusion systems. Initial research showed resazurin has a strong indicator of cytotoxicity and metabolic activity, even in 3D systems, as was evident by linear correlations of resazurin reduction with increasing time [78, 79]. However, the use of either AlamarBlue™ or Presto Blue™ to determine cellularity in 3D perfusion systems has been debated.

Research by Sonnaert showed that consistent results were seen when using resazurin reduction to determine cellularity in 2D, static 3D, and perfusion 3D systems [76]. This investigation used corrective factors to adjust for flow and diffusion. Other studies have found that resazurin assays in perfusion systems did correlate to cellularity, but only under certain conditions. Zhou saw that greater linearity was seen for proliferating cells as opposed to cells that had reached maximal cell density [80]. However, in a study completed Uzarski, the proliferation phase of cells had a large effect on the assay due to the available concentration of reagent in the system, leading to skewed cellularity results at higher cell densities [81]. Lastly, it has been seen that, when compared to DNA assays, resazurin based assays show inconsistent results for cellularity for multiple cell types [82].

1.10.4 Complex Permittivity

Complex permittivity is a methodology comparable to dielectric spectroscopy, specifically oriented towards tissue engineered constructs. Initial studies showed that complex permittivity measurements are able to determine the porosity of scaffolds, scaffold defects, and the presence of cells within a 3D scaffold [83]. Even more, morphological differences in cells can be evaluated, thereby indicating the extent of differentiation of stem cells [84]. However, this approach has encountered issues with defining the effects of extracellular matrices on the permittivity readings [84].

1.10.5 Monitoring Techniques Summary

Many of these techniques neglect to account for system dependent characteristics such as flow rate of media through the tissue engineered construct and the type of scaffold used. As such, these monitors are very system specific, and have little control in alternative systems. This highlights the importance of developing widely applicable correctional factors for cell specific characteristics such as oxygen uptake rate and glucose uptake rate, as these traits are central to determining tissue engineered construct characteristics in a non-destructive manner.

1.11 Effects of Oxygen on Cell Behavior

Oxygen tension has been shown to have a significant effect on cell behavior, especially in differentiating cells [85-87]. In the broadest sense, oxygen uptake rates by cells varies greatly depending on oxygen availability. In static systems, oxygen delivery is completed through diffusion alone, causing significant gradients for any system seeded with cells in a manner comparable to 3D constructs [85, 88]. For 2D systems, where diffusion though a scaffold is not a

factor, stem cells were shown to model Michaelis-Menten kinetics in oxygen uptake rates with varying oxygen concentrations [89]. Studies determining the effects of hypoxic and normoxic conditions on mesenchymal stem cell behavior show that hypoxia causes a decrease in the cells ability to differentiate [86, 87]. Even more, extended culturing of stem cells in hypoxic conditions has been shown to maintain undifferentiated state of these cells [87]. The reasoning for this likely centers on oxidative phosphorylation, as stem cells experiencing differentiation have a marked shift to oxidative phosphorylation for production of ATP from other metabolic pathways [86, 90]. This shift to oxidative phosphorylation is associated with mitochondrial biogenesis and reliance on glutamine availability [90, 91]. Oxygen uptake rate is also correlated with oxygen availability in perfusion systems, where increased superficial flow velocity correlated with increased oxygen uptake rates [92]. Furthermore, perfusion systems where oxygen gradients were below 5% were shown to still produce viable cells after two weeks in culture [93].

1.12 Summary of Goals

By monitoring the relationship present between oxygen uptake rate and oxygen availability, predictive models can be developed to determine the optimal flow rates for specific cell types, the potential effects of scaffold geometries, and the final construct characteristics through traditional oxygen and glucose monitoring techniques for a flow perfusion system. These models will take into account residence time of media in the construct, as this quality can more easily be applied to other 3D bioreactor systems. This will ultimately allow for cellularity and differentiation models to be expanded further, as different tissue engineering goals will require different bioreactor and scaffold types.

1.13 Objectives and Scope of Project

The primary objective of this investigation is to determine the effects of flow rate on oxygen uptake rate in non-differentiating mesenchymal stem cells. This objective involves characterizing the flow present within the flow perfusion system, and developing predictive models for cellularity and oxygen uptake rates based on flow.

Furthermore, oxygen uptake rate in mesenchymal stem cells in 2D systems has been shown to follow Michaelis-Menten kinetics, but current studies show that the behavior of cells and their uptake rates differ drastically in a 3D flow perfusion environment. It is a goal of this investigation to understand these differences in cell behavior as an aid designs for future bioreactors and monitoring systems in tissue engineering applications.

2. Methods

2.1 Cell Culture

Rat mesenchymal stem cells (rMSC) were used for all experiments conducted. Cells were extracted from the bone marrow of rat femurs and tibias using methods approved by the University of Oklahoma Institutional Animal Care and Use Committee (IACUC). Rats used were 6 week old male Winstar rats weighing approximately 175-199 grams (Envigo; Hsd:Wi). To isolate rMSCs, bone marrow from femur and tibia of rear legs was first extracted and suspended in α-Minimum Essential Media (αMEM; Sigma Aldrich) that was supplemented with 10% Fetal Bovine Serum (FBS; Atlanta Biologicals), and then distributed evenly into T75 cell culture flasks and allowed to incubate (37°C, 95% humidity, 5% CO_2) for 4 days. Cultures were then gently rinsed with phosphate buffered saline (PBS; Sigma-Aldrich) to remove non-adherent cells. Remaining cells were considered passage zero rMSCs, and were either passaged for immediate use or placed into cryogenic storage.

All cell cultures and bioreactors used αMEM supplemented with 10% FBS and 1% antibiotic/antimycotic (Life Technologies). Prior to seeding in the bioreactor, cells were incubated at 37°C, 95% humidity, and 5% CO_2 until they reached 80% confluency, at which time they were lifted using trypsin (Sigma-Aldrich), centrifuged at 1100 RCF for 5 minutes to create a cell pellet, suspended in αMEM, and distributed into T75 cell culture flasks at a concentration of 375,000-500,000 cells per flask. During expansion of cells, media was changed every other day. All studies were completed with cells at passage two.

2.2 Scaffold Production and Preparation

Spunbonded fiber scaffolds were utilized due to their high seeding efficiencies and reproducibility, and were made in accordance with previously published procedures [94]. These fibers were composed of randomly arranged poly(l-lactic acid) (PLLA) fiber layers that were stacked and compressed to form a sheet of 20 μm diameter fibers with approximately 85% porosity. PLLA (NatureWorks LLC; grade 6251D; 1.4% D enantiomer; MW=108,500 kDa) pellets were used to produce the fibers. Scaffold disks approximately 1.25 mm in height and 8 mm in diameter were cut from sheets of spunbonded fibers for use in bioreactor systems. 4 individual scaffold disks were used per cassette, creating a single scaffold approximately 5 mm in height and 8 mm in diameter.

Following ethylene oxide sterilization (AnPro 74i^{TM}), scaffold disks were placed into 95% ethanol and a vacuum was pulled on the container to purge air from the interior of the scaffolds. Once all air had been removed from the scaffold disks, they were submerged in sterile PBS to leach out remaining ethanol. Scaffold disks were then placed in αMEM supplemented with 50% FBS, and placed into the incubator for two hours prior to seeding to facilitate cell attachment.

2.3 Bioreactor Setup and Seeding

Bioreactor bodies were assembled prior to cell seeding. Assembly involved placing the cassette into the bioreactor body and connecting tubing to the reservoir system. Cassettes used are cylindrical containers that hold scaffolds in the bioreactor body. Furthermore, they have rubber seals at the top and bottom to ensure flow passes through the scaffolds, and not around the periphery of the cassette. **Figure 1** shows a diagram of the bioreactor body, cassette, and scaffold

setup. The system was purged of air in the biological hood by flowing media through the system. It was then allowed 4 hours to reach an equilibrium temperature of 37°C in the incubator. To prepare cells for seeding, they were first lifted and centrifuged to create a cell pellet, and then suspended in αMEM at a concentration of 2 million cells per 150 μL.

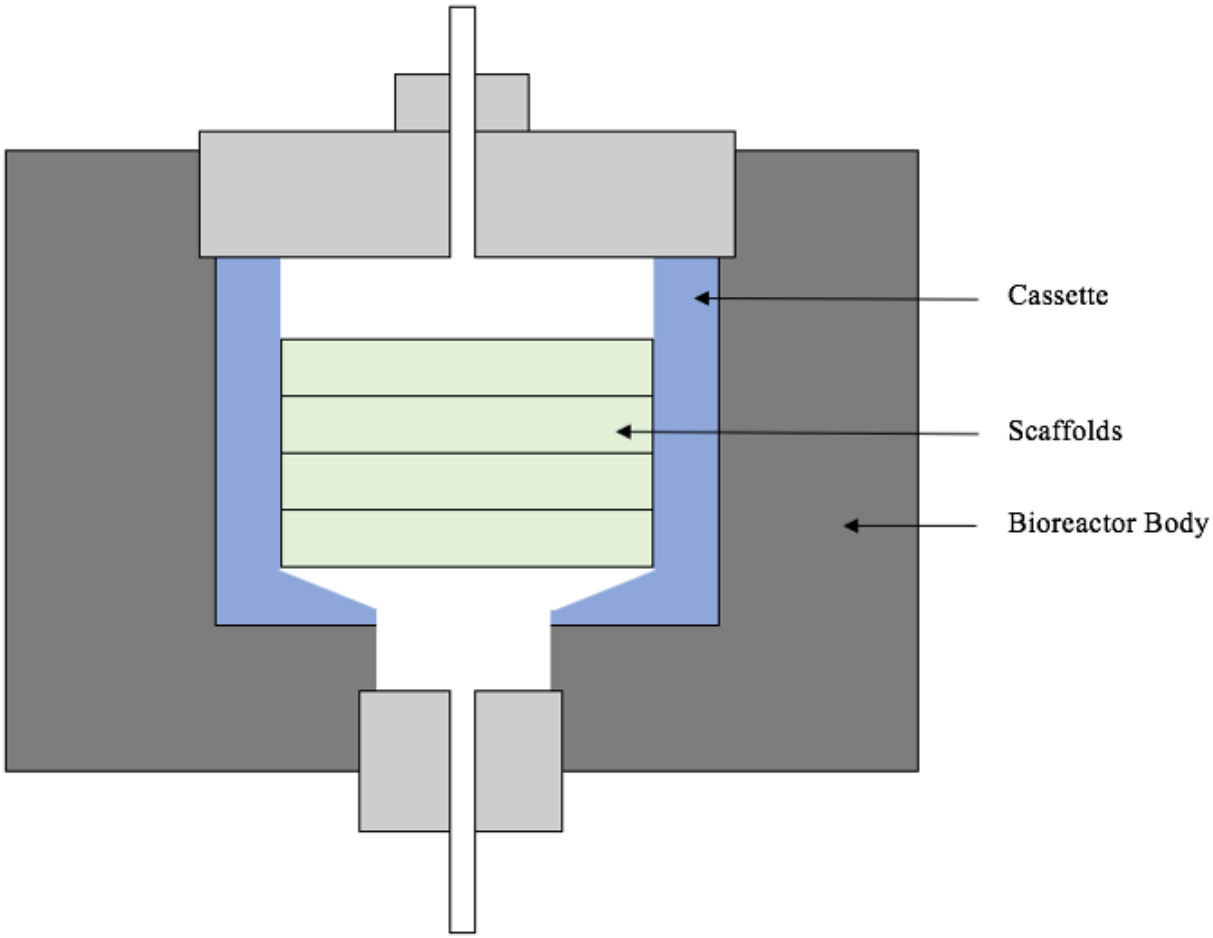

Figure 1: Cross-sectional View of Bioreactor
Cassette fits into bioreactor body, and contains a tapered bottom to ensure consistent positioning of scaffolds. Four scaffold disks were used for each construct. Media was perfused from the top of the bioreactor body, through the scaffolds, and out the exit at the bottom.

To complete the seeding, two individual scaffold disks were placed into the cassette, 75 μL of the cell suspension was pipetted onto the scaffolds, another single scaffold disk was placed into the cassette, 75 μL of the cell suspension was pipetted onto the scaffold disk, and finally the

last scaffold disk was placed into the cassette. Immediately following seeding of each construct, the bioreactors were placed into the incubator where a modified version of oscillatory seeding was completed. The flow of media through the construct was first allowed to flow in the forward direction at 150 μL/min for 1 minute, and was then reversed and allowed to flow in the backward direction at 150 μL/min for 1 minute. This was completed for 30 minutes, ending in the reverse direction. Following the oscillatory seeding procedure, the cells were allotted 2 hours to adhere to the scaffolds, wherein no flow was present in the system. The entire volume of media in the bioreactor and reservoir systems was then replaced to remove un-adhered cells from the system.

2.4 Oxygen Data Collection

The method by which oxygen concentrations were collected revolved around the use of RedEye^{TM} oxygen sensing patches (Ocean Optics). These patches were contained within an oxygen sensing module (OxyMod), originally developed by Simmons et al. [65]. Media was found to be saturated at the entrance to each cassette, so oxygen concentrations were measured at the exit of the bioreactor body to determine total oxygen consumed by the cells. Each of the OxyMod sensors was calibrated to 0.173 mmol O_2/L and 0 mmol O_2/L concentrations in deionized water prior to each setup. The sensors contained a material integrated into the sensor matrix. This material contained two fluorescent molecules, ruthenium and Pt-porphyrin complexes [95]. The fluorescence of this material is correlated to the oxygen concentrations in the media [95]. A fiber optic probe emitting blue light at 450 nm excited the material, and the resulting fluorescence was captured using the same probe. This data was then transferred to the NeoFox Viewing System^{TM}, and fluorescence data was related to the oxygen concentration in media using the Stern-Volmer equation [95].

Oxygen data was collected once, 2 days after initial seeding. Prior to data collection, all bioreactors were run at 150 μL/min. To complete data collection, the desired flowrate was adjusted and allowed to reach equilibrium for 45 minutes. Immediately following the 45-minute time period, oxygen data was collected for the exiting stream of each construct. The flow was then changed to the next flow rate, and another 45 minutes was allotted to reach equilibrium. The flow rates tested were 150 μL/min to 750 μL/min, increasing by 150 μL/min for each trial. All testing was completed within 3 hours, so the effects of cell proliferation were assumed to be zero. As non-differentiating media was used, it was assumed that flow rate, and the resulting shear stress changes, would have no effect on the oxygen uptake rate change as seen in differentiating cells. As a precaution, samples were collected both for flow rates incrementally increasing from 150 μL/min to 750 μL/min and for flow rates incrementally decreasing from 750 μL/min to 150 μL/min.

Readings taken from the NeoFox Viewing System™ were oxygen saturation values ranging from 0% to 100%, where 100% was the maximum oxygen saturation for media calculated using Henry's Law. The percent saturation values for the exiting stream were used to find the concentration of oxygen in the exiting stream, and this value with the flowrate was used to determine the oxygen uptake rate (OUR) for the construct (**Equation 2.1**).

$$OUR_{Construct} = \left(C_{O_2,in} - C_{O_2,out}\right) * Q \qquad \boldsymbol{Equation\ 2.1}$$

Where:

$$C_{O_2,in} = \text{Entering oxygen concentration } \left(\frac{\mu\text{mol}}{\text{L}}\right)$$

$$C_{O_2,out} = \text{Exiting oxygen concentration } \left(\frac{\mu\text{mol}}{\text{L}}\right)$$

$$Q = \text{Volumetric Flow Rate } \left(\frac{\text{L}}{\text{hr}}\right)$$

The OUR of the construct was then used to find the OUR on a per cell basis. Zero order kinetics were assumed to find an average OUR value per cell, in accordance with **Equation 2.2**.

$$OUR_{cell} = \frac{OUR_{construct}}{N_{cell}} \qquad \textbf{\textit{Equation 2.2}}$$

Where:

$$N_{cell} = \text{Number of cells}$$

2.5 Cellularity Quantification

Immediately following all oxygen data collection scaffolds were removed from each cassette, gently rinsed with sterile PBS, and placed into individual microcentrifuge tubes containing 1 mL nanopure water. Each scaffold was subjected to 3 freeze/thaw cycles utilizing a freezer at -20 °C. Freeze thaw cycles were completed over two days, where samples were frozen for 12 hours, thawed, and refrozen. The resulting mixture constituted the cell lysate for each sample taken. The cell lysate was used to determine the total number of cells adhered to the scaffold of each cassette. A double stranded (ds) DNA assay with standards (Quant-iT PicoGreen dsDNA Assay; Life Technologies) was completed to determine the total amount of DNA within each scaffold. 43 μL of the sample or standard was first pipetted into a 96 well plate. Standard solutions were made at concentrations ranging from 0.1 to 3 μg DNA per mL. Then 257 μL of a buffer and PicoGreen solution (10 mM Tris-HCl, 1 mM EDTA, pH 7.5, 0.75 μL PicoGreen Dye) was pipetted into each well, and the plate was incubated at room temperature in the dark for 5 minutes. The fluorescence was then read at an excitation wavelength of 495 nm and an emission wavelength of 520 nm. The standards were used to determine the amount of DNA in each sample. This amount of DNA was then associated with a particular cellularity, on the basis of

knowing the DNA content of each individual cell. For undifferentiated rMSCs, it was assumed that 4.5 picograms of DNA were contained in a single cell [96].

2.6 Residence Time Analysis

A residence time distribution function was derived from experimental data and subsequently integrated to determine the residence time for each flow rate tested in the bioreactor setup. Experimental design was adapted from work completed by Simmons [96]. A step input system was utilized for all tests completed, whereby DI water initially filled the system. A dye solution containing Trypan Blue (0.4% in Solution; Sigma) was then pumped through the scaffold and cassette combination, and the exiting stream was analyzed for dye composition (**c(t)**). To do this, absorbance measurements at 590 nm were taken of the elute, and compared to an absorbance measurement of 100% dye solution prior to passing through the system ($\mathbf{c_0}$). Breakthrough time ($\mathbf{t_{bt}}$), the time at which dye was first detected in the elute, was recorded. Samples were then collected every 30 seconds, and data collection stopped after the elute reached 99% of the initial concentration of dye, with the final reading constituting the final time point ($\mathbf{t_f}$). This data was then fit to **Equation 2.3** [96]**. Equation 2.3** has previously been shown to fit closely the concentration profiles produced by the residence time distribution analysis.

$$c(t) = \left(c_0 - \frac{c_0}{1 + \left(\frac{t - t_{bt}}{C_1}\right)^{C_2}} \right) * (1 - W) + c_0 * W \qquad \textbf{Equation 2.3}$$

Where:

$$W = \frac{t - t_{bt}}{t_f - t_{bt}}$$

$$C_1 \; and \; C_2 = \text{Curve fitting parameters}$$

A least squares regression was conducted to fit experimental data to **Equation 2.3**. The resulting formula was then utilized to determine the cumulative distribution function, F(t), and the residence time distribution function, E(t), shown by **Equations 2.4** and **2.5**.

$$F(t) = \frac{c(t)}{c_0} \qquad \textbf{Equation 2.4}$$

$$E(t) = \frac{\partial}{\partial t}F(t) = \frac{\partial}{\partial t}\left(\frac{c(t)}{c_0}\right) \qquad \textbf{Equation 2.5}$$

The residence time could be calculated by taking the following integral:

$$Average\ Residence\ Time = \tau = \int_0^{t_f} tE(t)dt \qquad \textbf{Equation 2.6}$$

A numerical integration was completed to determine the average residence time, and the resulting values for each flow rate were used for oxygen uptake rate analysis. Analysis was run 3 times per flow rate.

Experimental data was also used to determine the theoretical residence time for different reactor types that could potentially serve as a model for our bioreactor setup. For plug flow reactors, the residence time was determined using **Equation 2.7**.

$$Mean\ Residence\ Time = \tau_{plug} = \frac{Scaffold\ Void\ Volume}{Volumetric\ Flow\ Rate} = \frac{\pi * r^2 * h * \epsilon}{\nu} \qquad \textbf{Equation 2.7}$$

Where:

$$\nu = \text{Volumetric Flow Rate } \left(\frac{\text{mL}}{\text{sec}}\right)$$

$$r = \text{Scaffold Radius (cm)}$$

$$h = \text{Scaffold Height (cm)}$$

$$\epsilon = Porosity$$

The residence time for a tubular laminar flow reactor was also calculated after determining if the flow in the bioreactor system was laminar using the Reynolds number. The Reynolds number was found using **Equation 2.8.**

$$Reynold's\ Number = Re = \frac{\rho V d}{\mu} \qquad \textbf{Equation 2.8}$$

Where:

$$\rho = Fluid\ Density\ \left(\frac{kg}{m^3}\right)$$

$$V = Fluid\ Superficial\ Velocity\ \left(\frac{m}{sec}\right)$$

$$d = Scaffold\ Diameter\ (m)$$

$$\mu = Dynamic\ Viscosity\ \left(\frac{kg}{m * sec}\right)$$

Once the Reynolds number was determined, any value less than 2300 was considered laminar flow [97].

To determine the theoretical residence time for the laminar tubular reactor, the residence time distribution function was approximated using **Equation 2.9** [97]**.**

$$E(t) = \frac{\tau^2}{2 * t^3} \qquad \textbf{Equation 2.9}$$

Where:

$$\tau = 2 * Breakthrough\ Time\ (t_{bt})$$

$$t = Time\ (seconds)$$

The average residence time was then calculated using a numerical integration as shown in **Equation 2.6**.

Following residence time analysis, a visual study was completed to determine the flow patterns within the construct. The Trypan Blue (MW=872.88 g/mol) dye solution was pumped through the scaffold until dye was initially seen in the effluent. Once dye was detected in the effluent, flow was stopped, and scaffold disk layers were removed from the cassette. As 4 stacked scaffold disks were used for all bioreactors and analysis run, these 4 scaffold disks were taken out and each layer was analyzed for dye present. This was completed to visually confirm flow geometries within the scaffold.

2.7 Statistical Analysis

Following data collection and analysis, a one-way ANOVA was conducted to determine if there was a significant effect (p-value < 0.05). If significance was incurred, a post hoc Tukey's test was run to find which individual groups were statistically significant.

3. Results and Discussion

Results are discussed in a stepwise manner, where analysis proceeds in the order which data was obtained. This aids in providing a comprehensive understanding of why the primary objectives of this project were completed and how they were analyzed.

3.1 Oxygen Concentration Drop

The concentration of oxygen entering and exiting the construct was used to determine the uptake rate by the constructs, and ultimately on a per cell basis. Prior to determining these values, the drop in media oxygen concentration having moved through the construct was measured.

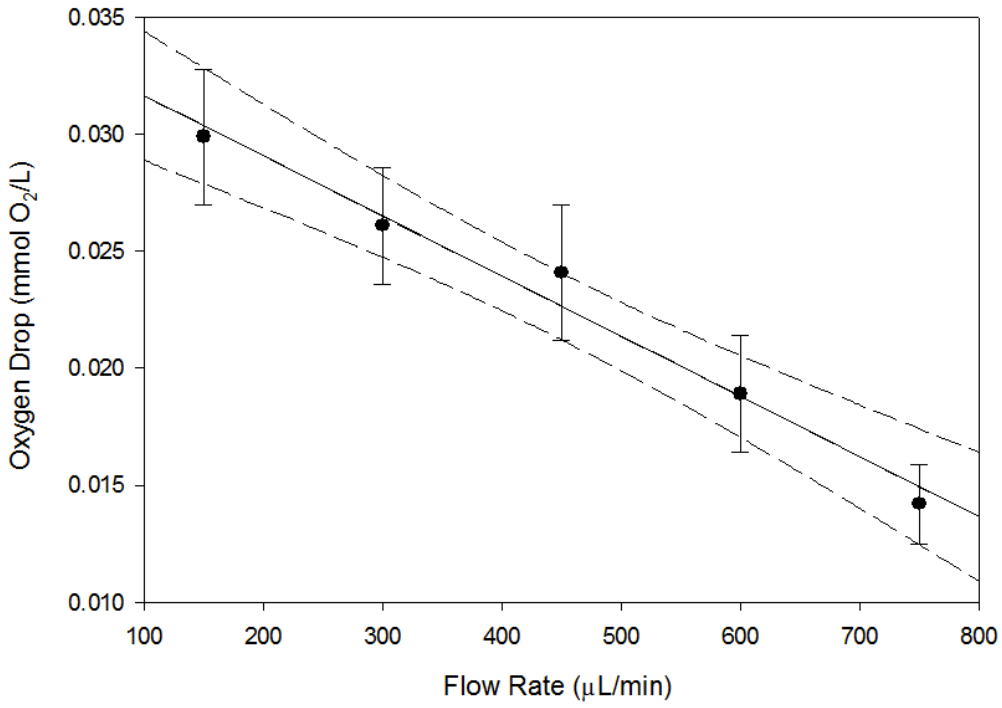

Figure 2: Oxygen Drop Across Construct
The total concentration drop in oxygen across the construct is shown in comparison to the flow rate. As flow rate was increased, a linear decrease in oxygen concentration drop across the construct can be seen. A linear regression was performed and a slope of $-2.6x10^{-5}$ was found with an R^2 value of 0.98. Dashed lines show the 95% confidence interval for the linear regression analysis. Error bars represent mean ± SEM. A sample size of n=8 was used for analysis.

As flow rate of media through the construct increased, a linear decrease in oxygen drop was observed. **Figure 2** shows this decreasing trend. As flow rate increases, larger amounts of oxygen are delivered to the cells within the construct. It is expected that the concentration of oxygen in media leaving the construct would increase, thereby yielding a lower net change in oxygen concentration. These values of oxygen concentration were then used to determine the rate of oxygen consumed by the entire construct.

3.2 Oxygen Uptake Rate Per Construct

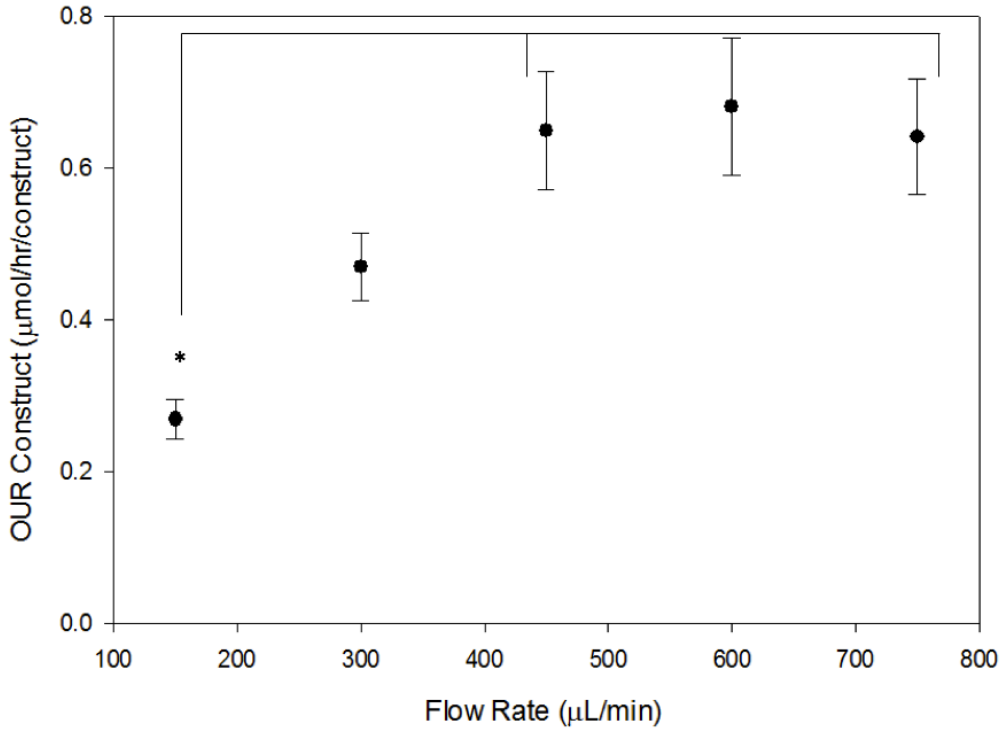

Figure 3: Oxygen Uptake Rate per Construct
Oxygen uptake rate on a per construct basis is shown as flow rate is changed. As flow rate increased, a linear increase in oxygen uptake rate for the construct was initially observed. After a flow rate of 450 µL/minute was reached, the uptake rate plateaued at approximately 0.65 µmol/hr/construct. Error bars represent mean ± SEM. A sample size of n=8 was used for analysis. ANOVA with Post-hoc Tukey's test completed to calculate significance "" ($p < 0.05$).*

To determine the total amount of oxygen consumed by the construct, the oxygen drop across the construct was multiplied by the flowrate, giving a time dependent value of oxygen consumption by the construct, as a whole. **Figure 3** shows an initial linear trend for the uptake rate, which proceeded to plateau at approximately 0.65 μmol/hr/construct. While these values of oxygen uptake rate are indicative of the general trends expected for oxygen uptake rate, they are unable to form a predictive model for cellularity. As it is unknown what effects flow may have, it was important to determine the oxygen uptake rate on a per cell basis for each flow tested. These values of oxygen uptake rate were divided by the respective cellularity of that construct to determine the oxygen uptake rate per cell.

3.3 Cellularity Quantification

Construct analysis yielded cellularity values for use in oxygen uptake rate analysis. A single bioreactor setup was used for all ensuing experiments. All constructs were analyzed for DNA quantity, and this DNA concentration was used to determine the cellularity of the construct by dividing the total DNA by 4.5 picograms DNA per cell for non-differentiating MSCs. An average cellularity of **224,069 ± 18,410** cells was used for analysis. **Figure 4** presents a box and whisker graph that shows the average readings for cellularity with interquartile ranges indicated by upper and lower boundaries of box, media cellularity value indicated by the center line, and maximum and minimum values indicated by error bars. The upper and lower edges of the shaded box indicate the first and third quartile ranges, respectively.

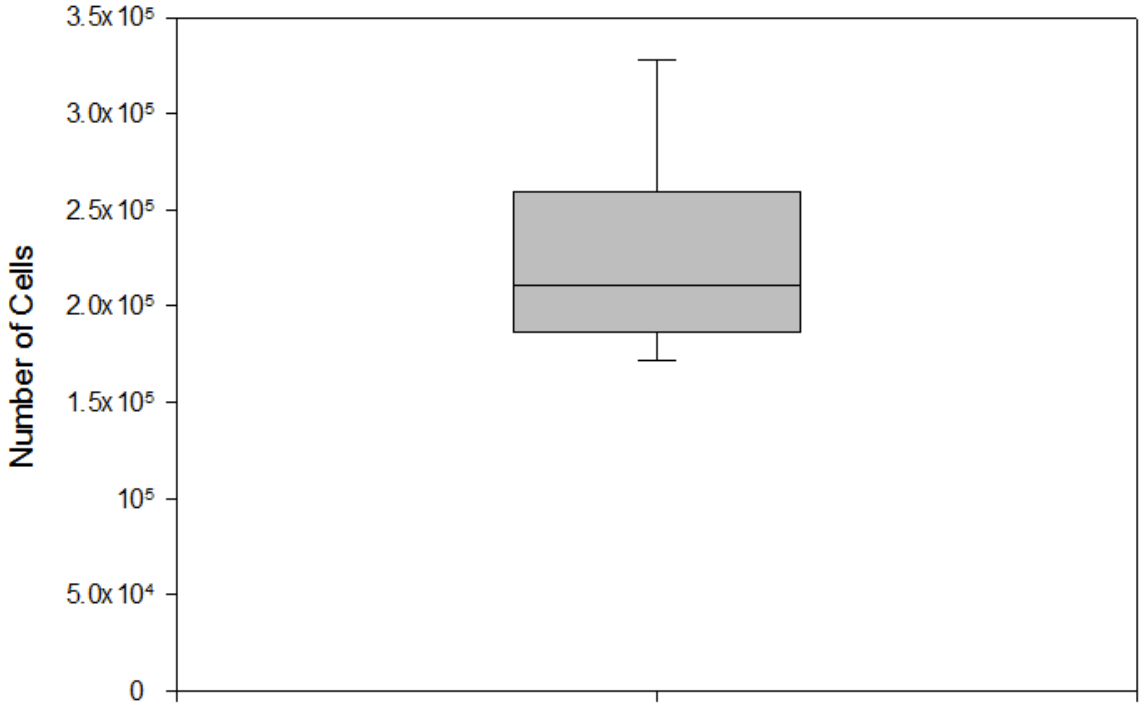

Figure 4: Construct Cellularity
Eight constructs were analyzed for DNA quantity, and that DNA quantity was associated with a cellularity. The box and whisker plot shows the 1st and 3rd quartile ranges, the median cellularity (indicated by line in the center of the plot), and the maximum and minimum values (indicated by the error bars).

3.2 Oxygen Uptake Rate Per Cell

Oxygen uptake rates on a per cell basis show comparable trends to overall construct uptake rates. These rates initially see a linear increase, followed by a plateau at approximately 3 picomoles O_2/hr/cell. These values for oxygen uptake rate are consistent with values obtained by Simmons et al. in 3D perfusion bioreactor systems, but still an order of magnitude greater than other literature values [65]. In 3D systems, oxygen uptake rates for undifferentiated cells were approximately 1.5 picomoles O_2 /hr/cell at flow rates of 150 μL/min [96]. However, in 2D systems, the maximum oxygen uptake rate was approximately 0.1 picomoles O_2/hr/cell [89]. The plateau reached at 450 μL/min indicates that non-differentiating mesenchymal stem cells will

ultimately reach a maximum value of oxygen consumption, reaching a value that is on-par with differentiating stem cells in other perfusion systems. **Figure 5** potentially indicates this relationship is solely flow based, but it is important to characterize the flow within the scaffold to determine the root cause of these trends.

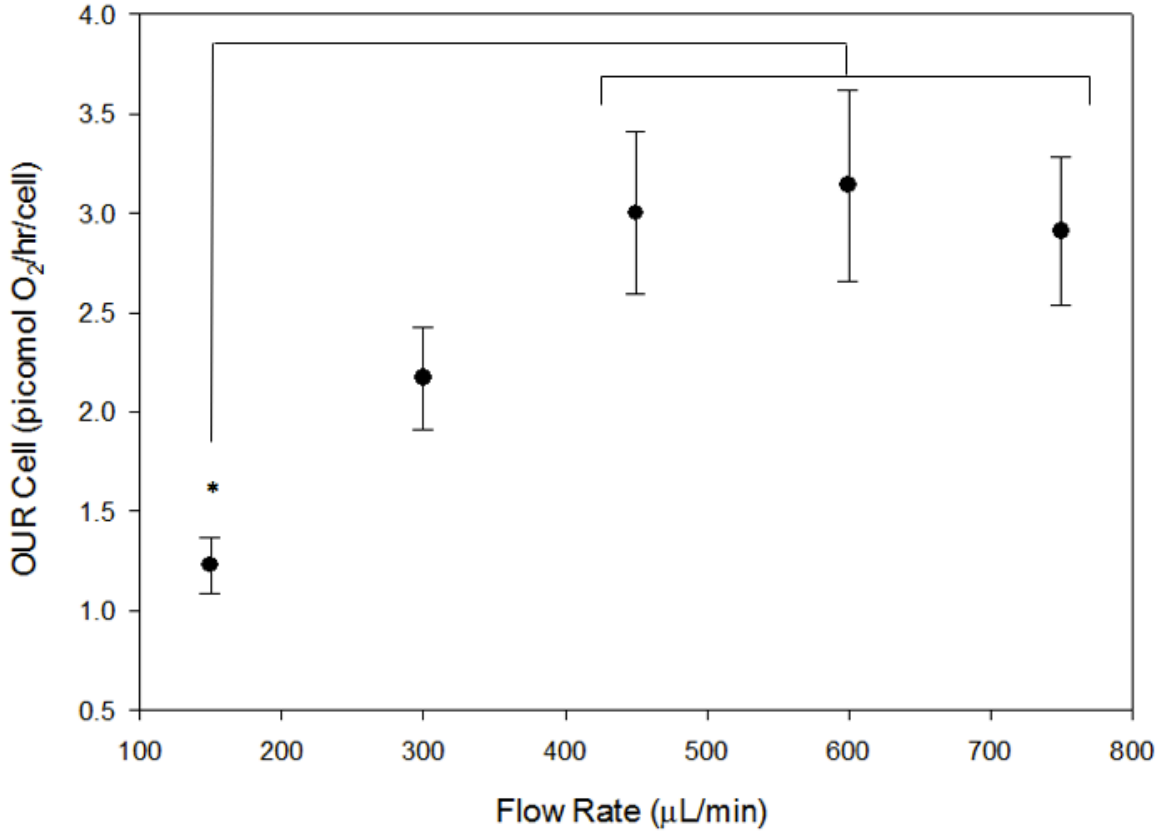

Figure 5: Oxygen Uptake Rate per Cell
The oxygen uptake rate on a per cell basis is shown in comparison to the flow rates tested. As flow rate increased, a linear increase in oxygen uptake rate on a per cell basis was observed. After a flow rate of 450 µL/minute was reached, the uptake rate plateaued at about 3.0 picomol O_2/hr/cell. Error bars represent mean ± SEM. A sample size of n=8 was used for analysis. ANOVA with Post-hoc Tukey's test completed to calculate significance "" ($p < 0.05$).*

3.5 Residence Time Distribution Analysis

The residence time was analyzed by evaluating effluent leaving the bioreactor system. In **Table 1** the values and constants required for **Equation 2.3** are outlined. Using these values, the experimentally derived values for mean residence time are listed in **Table 2**. These residence times decrease with increasing flow rate. To aid in characterizing the flow in these systems, the normalized residence time distribution function was compared to literature graphs for plug flow and laminar tubular flow reactors in **Appendix A.2**. Additional analysis was done, whereby experimentally obtained values for breakthrough time and time at which effluent concentration reached 99% of original concentration were used to determine the theoretical mean residence time for laminar tubular flow reactors with fully developed flow. Experimentally obtained values were also compared to theoretical values of residence time for plug flow reactors. These comparisons are seen in **Figure 6.** Studies were completed in the absence of cells.

Table 1: Fitted Equation for Experimentally Obtained Data

Experimentally obtained values and constants for fitted equation are shown. These values were collected for each flow rate tested. t_{bt} is the breakthrough time of dye leaving the cassette; t_f is the time at which experimentally obtained concentrations of dye leaving the cassette reach 99% of c_o; C_1 and C_2 are fitted constants for each flow rate, determined by a least squares regression. Fitted constants are shown for each run completed: 3 for each flow rate.

Flow Rate (μL/min)	**t_{bt} (seconds)**	**t_f (seconds)**	**C_1**	**C_2**
150 – 1	103	1350	117.041	1.112
150 – 2	180	1290	8.898	0.379
150 – 3	167	1170	15.253	0.310
300 – 1	63	810	10.618	0.588
300 – 2	71	990	42.416	0.703
300 – 3	93	870	28.218	0.703
450 – 1	71	825	2.706	0.544
450 – 2	39	795	1.438	0.303
450 – 3	59	465	40.001	1.125
600 – 1	47	795	28.468	1.249
600 – 2	46	795	10.365	0.786
600 – 3	47	495	28.209	1.237
750 – 1	29	585	4.043	0.462
750 – 2	47	585	23.718	1.326
750 – 3	40	495	14.715	0.890

Table 2: Mean Residence Time Values
Residence time for each flow was calculated 3 times using the aforementioned equation and the trapezoid numerical integration technique. Averages of these values are shown ± SEM. A sample size of n=3 was used for analysis.

Flow Rate (μL/min)	Ave. Residence Time (seconds)
150	*247* ± 17.6
300	*149* ± 20.8
450	*91* ± 14.2
600	*89* ± 6.3
750	*72* ± 5.3

Prior to calculating the theoretical time for laminar tubular flow reactors, it was important to verify that flow within the bioreactor system for all flow rates was laminar. Reynolds numbers were calculated for each flow rate, under the assumption the media solution maintained similar viscosity and density values as water. The cutoff for laminar and turbulent flow can be approximated in packed bed reactors. Laminar flow is considered any value less than 1, the transition phase is from 1 to 100, and a Reynolds number greater than 100 is considered turbulent [98]. **Table 3** shows that all calculated Reynolds numbers are at the cutoff for laminar flow, thereby showing that flow in the reactors is likely laminar. Furthermore, due to the high porosity of the scaffold, the cutoffs are likely lower than that for a typical packed bed reactor.

Table 3: Reynolds Number Values
Reynolds Number for each flow was calculated using ***Equation 2.8.*** *All calculated values are at or below 1, but well below 100, indicating laminar flow through construct.*

Flow Rate (μL/min)	Reynolds Number
150	*0.6*
300	*1.2*
450	*1.8*
600	*2.4*
750	*3.0*

The residence times values for laminar flow, plug flow, and experimentally obtained values is shown in **Figure 6**, where experimental values can be compared directly to what would be expected for each of these reactor types operating under the designated flow conditions. Experimental values are nearly identical to those found for laminar tubular flow reactors, and nearly 4 to 8 times the values obtained for plug flow reactors with no dispersion. Previous experiments showed that this bioreactor system was comparable to plug flow with significant dispersion effects, however, comparisons to theoretical values indicate that it is much closer to residence times seen in fully developed laminar flow with little to no dispersion [96]. It is important to note that these theoretical values are calculated for reactors with no porous medium, which differs slightly from the current setup that contains an 85% porous scaffold.

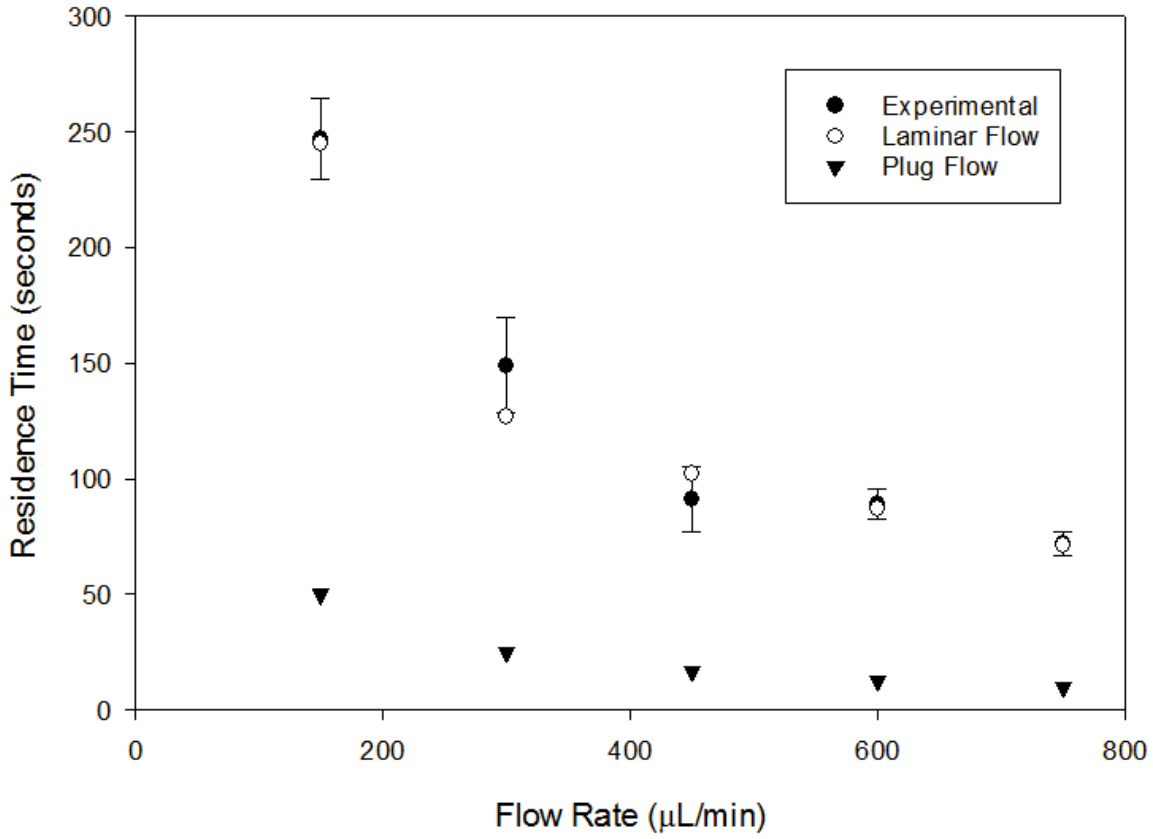

Figure 6: Theoretical Residence Time Comparison
Theoretical values for residence time were computed for laminar tubular reactors and plug flow reactors, and then compared to experimental values. Plug flow values are significantly lower than experimental values, and laminar tubular reactors are very similar to experimentally obtained values. Error bars represent mean ± SEM. A sample size of n=3 was used for analysis.

These claims are further supported by the normalized residence time distribution function graphs in **Appendix A.2**. These graphs show the characteristic spike, followed immediately by a gradual decrease in the function. The presence of a scaffold, and the resulting porosity, were thought to have an effect on these trends. However, it may be safe to assume that since the scaffold porosity is so large ($\epsilon = 0.85$) it has negligible effects on the flow characteristics. Furthermore, the assumption of fully developed flow could be indicative of significant gradients in the radial direction, something not taken into account in previous models.

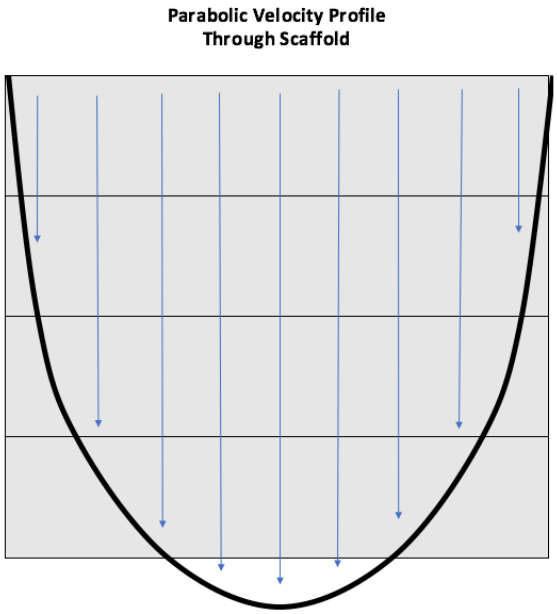

Figure 7: Theoretical Flow Velocity Profile
Scaffold disk layers are shown, where top is where flow enters cassette. Theoretical flow velocity profile associated with fully developed flow, showing how fluid would move through scaffold.

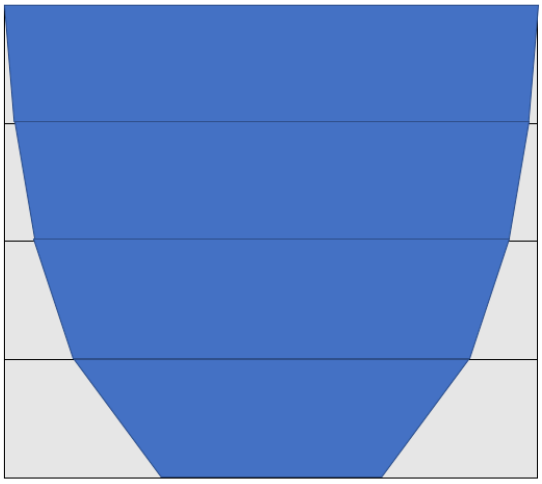

Figure 8: Anticipated Cross-sectional Dye Profile
Assuming flow follows fully developed laminar flow through scaffolds, initial dye should be distributed through scaffold in the manner described above. The scaffold disks at the entrance are well saturated by dye, and dye continues to move in higher rates through the center of the scaffold.

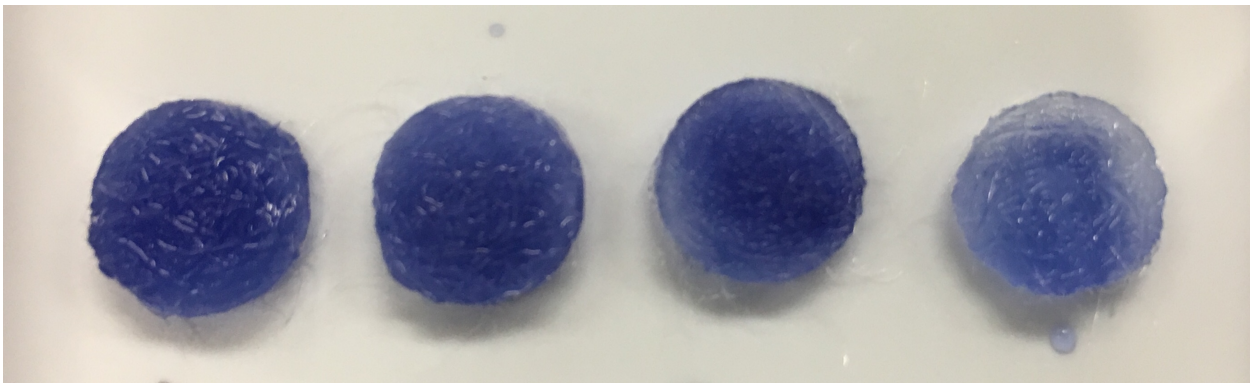

Figure 9: Dye Composition per Scaffold Disk Layer
Moving from left to right, scaffold disks are placed from the top of the cassette near the entrance towards the exit of the cassette. The saturation of dye in the scaffold is indicative of a fully developed profile, seeing as the top scaffold disk is fully saturated in dye, and moving towards the bottom the dye is more concentrated in the center of the scaffold disk. Tested at 750 μL/min.

Fully developed flow in pipes is characterized by a signature parabolic velocity profile (See **Figure 7**), where high flow rates are present in the center of the tube and decrease towards the sides. In the event this profile was present in the construct, it would be indicative of significant gradients in the radial direction. **Figure 8** shows what initial dye saturation in the scaffold disk layers might look like if this type of flow was present in the bioreactor system, where scaffold disks near the top are nearly saturated with dye, and saturation becomes increasingly concentrated in the center of the construct moving downward.

Figure 9 shows the dye initial concentration of dye each layer of the scaffold immediately following the flow of dye into the system up until the breakthrough time. Scaffold disks were stacked in bioreactor, consistent with **Figure 1**, and subsequently removed from cassette and laid side by side, where the leftmost scaffold constitutes the top scaffold in the cassette. These results are consistent with the expected dye profile in **Figure 8**, further supporting the claim that fully developed laminar flow is present in the bioreactor system. Additionally, these results show the presence of gradients in the radial direction.

3.6 Oxygen Uptake Rate Relative to Residence Time

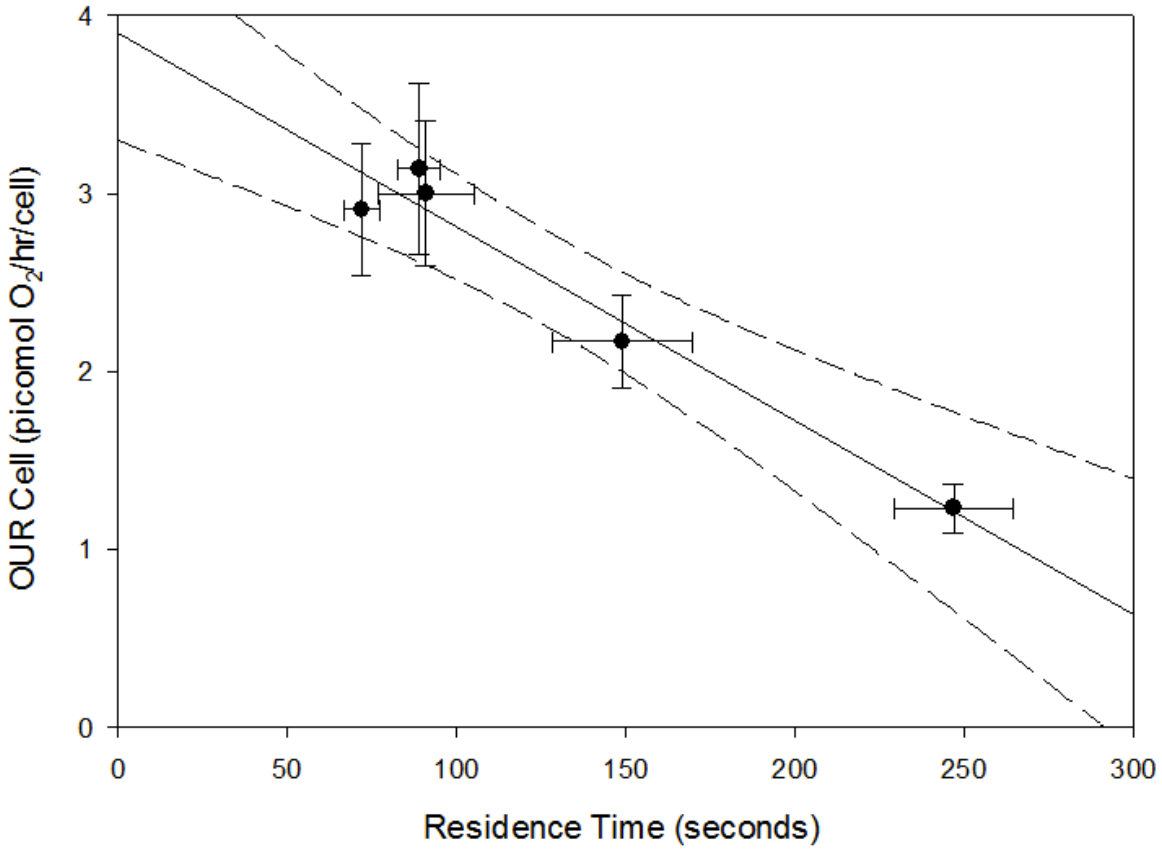

Figure 10: Oxygen Uptake Rate per Cell vs. Residence Time
Oxygen uptake rate on a per cell basis is shown in comparison to the residence time experienced at the associated flow rate. The relationship between residence time through the reactor at a particular flow rate and the OUR per cell at that flow rate indicates a linear relationship. A linear regression was performed. A slope of -0.0109 and a y-intercept of 3.899 were found with an R^2 value of 0.96. Dashed lines show the 95% confidence interval for the linear regression analysis. Error bars represent mean ± SEM. A sample size of n=8 was used for analysis for OUR Cell. A sample size of n=3 was used for analysis for Residence Time.

In place of flow rate, residence time was graphed against the oxygen uptake rate on a per cell basis in **Figure 10.** The graph shows a linear relationship between the two variables, demonstrating a direct relationship between residence time of media in the bioreactor system and the uptake rate of oxygen by cells. A linear regression was performed, and a R^2 value of 0.96 was found. A 95% confidence interval for the linear regression was graphed, and shows a high

level of accuracy for the predictive model. The slope and y-intercept were used to create a model (**Equation 3.1)** that relates the residence time to the cellular oxygen uptake rate in **Figure 11.**

$$OUR\ Cell\ \left(\frac{picomole\ O_2}{hr * cell}\right) = -0.0109 * \tau + 3.899 \qquad \boldsymbol{Equation\ 3.1}$$

Where:

$$\tau = \text{Mean Residence Time}$$

Figure 10 also shows the potential for a maximum oxygen uptake rate for mesenchymal stem cells in a reactor as the residence time approaches zero, given as the y-intercept of the model. As stated previously, fully developed laminar flow accurately models the flow patterns within the bioreactor system, indicating standard parabolic velocity profiles. Due to lower velocities at the edges of the scaffold and higher velocities at the center of the scaffold, low flow rates would result in low oxygen delivery to the edges of the scaffold. Since flow would pass primarily through the center of the construct, diffusion of oxygen would be the primary means of oxygen deliver to cells located at the periphery of the tissue engineered construct. As local concentration of oxygen is central to cellular oxygen uptake rates, it is safe to assume that cells at the periphery of the construct would consume lower amounts of oxygen than those at the center, resulting in a lower average oxygen uptake rate on a cellular basis. As flow rate increases, it is predicted convective mass transfer would slowly overtake diffusive mass transfer, resulting in greater deliver of oxygen to the cells. The greater availability of oxygen on a local level throughout the construct would result in higher overall levels of oxygen uptake, until cells reached their true maximum uptake rate. However, efforts to approach this limit cannot be accomplished, as cell detachment would likely occur prior to that point due to high shear at the surface of the cells with high flow rates.

3.7 Predicted Oxygen Uptake Rate Model

The predictive model for oxygen uptake on a cellular basis, given residence time for the construct, was graphed in **Figure 11** versus the experimentally obtained values for cellular oxygen uptake rate.

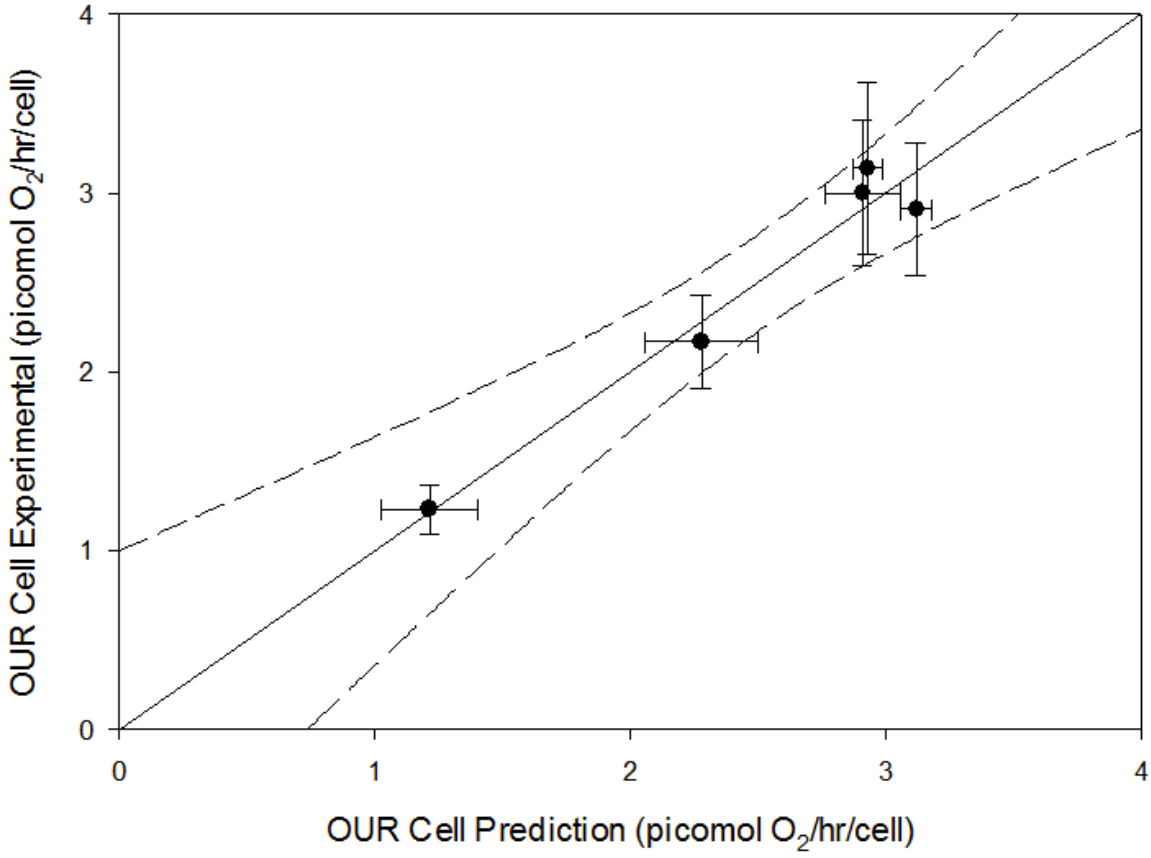

Figure 11: Oxygen Uptake Rate Prediction vs. Experimental
The predictive equation showing the relationship between residence time and OUR Cell was plotted against experimentally obtained values of OUR Cell for each flow rate tested. A linear regression was performed and a slope of 0.958 was found with an R^2 value of 0.96. Dashed lines show the 95% confidence interval for the linear regression analysis. Error bars represent mean ± SEM. A sample size of n=8 was used for analysis for experimental values. A sample size of n=3 was used for analysis for predicted values.

Equation 3.1 was used to predict oxygen uptake rates, and shows a strong relationship between residence time and oxygen uptake rates on a per cell basis. A linear regression for the model was completed, and a slope of 0.958 and R^2 value of 0.96 indicate a high potential for residence time, alone, to be an indicator oxygen uptake rate and hypothetically cellularity in the construct. The dashed lines in **Figure 11** represent the 95% confidence interval derived from the linear regression, and further show the fit of the predictive model. This behavior is likely driven by the mitigation of gradients to extending from the center to the periphery of the scaffold. As such, scaffold architecture would likely have a significant effect on these predictive models.

4. Conclusions

Analysis of flow effects within the 3D flow perfusion bioreactor system used for production of bone tissue engineered constructs yielded results that show the importance of flow characterization within bioreactor systems, in addition to displaying the effects of these flow characteristics on the behavior of mesenchymal stem cells. Previous work completed by Simmons predicted the flow within the bioreactor system to be well approximated by plug flow with dispersion effects [96]. This work championed these findings. It highlighted the importance of plug flow in mitigating radial effects of flow within the reactor system, stating that shear stress could evenly approximated across the cross-section of the construct [96]. However, new results show that the flow within the reactor could better be described as fully developed laminar flow, causing significant radial effects in terms of shear stresses experienced by cells and delivery of nutrients to these cells. The standard parabolic shape of laminar flow models in tubes show sharp declines in fluid velocity moving from the center of the construct to the periphery, producing these effects. Potential side effects of these large gradients could appear in the upregulation of certain genes in mesenchymal stem cells, such as Hypoxia Inducible Factor 1-α (HIF1α), which has been shown to be a key regulation in cell activity [99]. HIF1α has been shown to be a key player in proliferation, indicating that gradients could have drastic effects on construct viability [99]. It is important to note that these results were found for spunbonded PLLA fibers at high porosities, allowing for the possibility of flow characteristics to change in other bioreactor system and other scaffold types.

The cell specific oxygen uptake rates found in this experiment are an order of magnitude larger than those found in literature. This could potentially be caused by a multitude of factors. First, nearly all literature values obtained are found in 2D systems, finding maximum uptake

rates of approximately 0.1 picomoles oxygen/cell/hour, compared to our findings of 3.02 ± 0.07 picomoles oxygen/cell/hour [86, 89]. However, the effects of dynamic versus static culturing systems has been shown to have a significant effect on metabolic properties of mesenchymal stem cells in terms of glucose consumption [100]. These findings could be extrapolated to oxygen consumption, as well, since glucose and oxygen are the two primary indicators of metabolic rate. Additionally, cells could potentially vary metabolic rates in high confluency environments in 2D systems, where many of these oxygen uptake rate values were observed. Our system had comparatively low confluency, potentially yielding higher net oxygen uptake rates.

The overarching objective of this investigation was to determine a relationship between flow characteristics and oxygen uptake rate of cells. Our results found that a linear relationship existed between residence time and cell specific oxygen uptake rate. These results were also consistent with findings of laminar flow characteristics in our system, where higher convective mass transfer of oxygen, associated with lower residence time, caused higher oxygen uptake rates. These findings could be extrapolated using our model to determine a maximum oxygen uptake rate in conditions where there are no mass transport limitations, giving an absolute maximum cell specific oxygen uptake rate of approximately 4 picomoles/cell/hour. While these results would be impossible to reach, due to both limitations with flow effects on cells and mass transport limitations in nearly all systems, it could potentially provide insight to success of new bioreactor designs in terms of nutrient delivery to cells within a tissue engineered construct. The predictive model could also serve as a corrective factor for other systems relying on on-line oxygen measurements to determine cellularity.

5. Future Directions

This study has provided preliminary data highlighting the effects of flow characteristics in a bioreactor system on cell behavior. Furthermore, it has exposed weaknesses in current models used for nutrient delivery and shear stress analysis. In order to completely reap the benefits of flow analysis, it is necessary to account for other variables in tissue engineering bioreactor systems.

Initially, the flow rates tested were completed towards the lower end of flow rates previously used in this system. The current bioreactor design is capable of reaching 3 mL per minute. It would be important to observe oxygen uptake rates at these flow rates to determine if a maximum oxygen uptake rate of 3.02 ± 0.07 picomoles oxygen/cell/hour was truly reached. Furthermore, it could yield additional residence time analysis to conclude if flow characteristics within the bioreactor system change at maximum flow rates.

The effects of these oxygen concentrations on cell behavior needs to be studied. It would be important to determine if extended exposure to high oxygen availability will have any effects on regulation of processes within the cell. Additionally, it would be of interest to determine if the excess of oxygen could have an effect on the rate of differentiation of mesenchymal stem cells into osteoblasts.

These experiments for oxygen consumption would also need to be completed at varying cellularity and confluency within the construct. These models were reached using only one cell density, and cell density could potentially have a large effect on the metabolism of the cells and therefore the cell specific uptake rate. Since this would ultimately serve as a predictive measure for bone tissue engineered constructs, experiments would need to be completed for differentiating cells as they are known to increase oxygen consumption as they proceed through

osteoblastic differentiation. Scaffold geometries could also play a large role in flow characteristics throughout the constructs, so repeating residence time distribution analysis with varying scaffold geometries would further allow these results to be extrapolated to other bioreactor designs. Scaffold geometry could also play a large role in radial gradients, and give insight on how to mitigate them.

Literature Cited

1. Haugen, H.J., et al., *Bone grafts: which is the ideal biomaterial?* J Clin Periodontol, 2019.

2. Shin, S.R. and P. Tornetta, *Donor Site Morbidity After Anterior Iliac Bone Graft Harvesting.* Journal of Orthopaedic Trauma, 2016. **30**(6): p. 340-343.

3. Cancedda, R., P. Giannoni, and M. Mastrogiacomo, *A tissue engineering approach to bone repair in large animal models and in clinical practice.* Biomaterials, 2007. **28**(29): p. 4240-50.

4. Campana, V., et al., *Bone substitutes in orthopaedic surgery: from basic science to clinical practice.* Journal of Materials Science-Materials in Medicine, 2014. **25**(10): p. 2445-2461.

5. Roberts, T.T. and A.J. Rosenbaum, *Bone grafts, bone substitutes and orthobiologics The bridge between basic science and clinical advancements in fracture healing.* Organogenesis, 2012. **8**(4): p. 114-124.

6. Ashman, O. and A.M. Phillips, *Treatment of non-unions with bone defects: Which option and why?* Injury-International Journal of the Care of the Injured, 2013. **44**: p. S43-S45.

7. Sen, M.K. and T. Miclau, *Autologous iliac crest bone graft: should it still be the gold standard for treating nonunions?* Injury, 2007. **38 Suppl 1**: p. S75-80.

8. Buttermann, G.R., *Prospective nonrandomized comparison of an allograft with bone morphogenic protein versus an iliac-crest autograft in anterior cervical discectomy and fusion.* Spine Journal, 2008. **8**(3): p. 426-435.

9. Khan, S.N., et al., *The biology of bone grafting.* Journal of the American Academy of Orthopaedic Surgeons, 2005. **13**(1): p. 77-86.

10. Myeroff, C. and M. Archdeacon, *Autogenous Bone Graft: Donor Sites and Techniques.* Journal of Bone and Joint Surgery-American Volume, 2011. **93a**(23): p. 2227-2236.

11. Charles, M., et al., *Fat embolism following posterior iliac graft harvest for jaw reconstruction: managing the complications of major surgery.* J Can Dent Assoc, 2007. **73**(1): p. 67-70.

12. Wiese, A. and H.C. Pape, *Bone Defects Caused by High-energy Injuries, Bone Loss, Infected Nonunions, and Nonunions.* Orthopedic Clinics of North America, 2010. **41**(1): p. 1-+.

13. Maurer, S.G., A.C. Baitner, and P.E. Di Cesare, *Reconstruction of the failed femoral component and proximal femoral bone loss in revision hip surgery.* J Am Acad Orthop Surg, 2000. **8**(6): p. 354-63.

14. Charalambides, C., M. Beer, and A.G. Cobb, *Poor results after augmenting autograft with xenograft (Surgibone) in hip revision surgery - A report of 27 cases.* Acta Orthopaedica, 2005. **76**(4): p. 544-549.

15. Azi, M.L., et al., *Autologous bone graft in the treatment of post-traumatic bone defects: a systematic review and meta-analysis.* Bmc Musculoskeletal Disorders, 2016. **17**.

16. Muramatsu, K., et al., *Recalcitrant posttraumatic nonunion of the humerus: 23 patients reconstructed with vascularized bone graft.* Acta Orthop Scand, 2003. **74**(1): p. 95-7.

17. Heise, U., J.F. Osborn, and F. Duwe, *Hydroxyapatite ceramic as a bone substitute.* Int Orthop, 1990. **14**(3): p. 329-38.

18. Hettwer, W., *Synthetic bone replacement Current developments and perspectives.* Orthopade, 2017. **46**(8): p. 688-700.

19. Buser, Z., et al., *Synthetic bone graft versus autograft or allograft for spinal fusion: a systematic review.* Journal of Neurosurgery-Spine, 2016. **25**(4): p. 509-516.

20. Langer, R. and J. Vacanti, *Advances in tissue engineering.* J Pediatr Surg, 2016. **51**(1): p. 8-12.

21. Jaklenec, A., et al., *Progress in the tissue engineering and stem cell industry "are we there yet?".* Tissue Eng Part B Rev, 2012. **18**(3): p. 155-66.

22. Yin, S., et al., *Recent Advances in Scaffold Design and Material for Vascularized Tissue-Engineered Bone Regeneration.* Adv Healthc Mater, 2019: p. e1801433.

23. Sharma, D., et al., *Upgrading prevascularization in tissue engineering: A review of strategies for promoting highly organized microvascular network formation.* Acta Biomater, 2019.

24. Babilotte, J., et al., *3D printed polymer-mineral composite biomaterials for bone tissue engineering: Fabrication and characterization.* J Biomed Mater Res B Appl Biomater, 2019.

25. Bilezikian, J.P., L.G. Raisz, and G.A. Rodan, *Principles of bone biology*. 1996, San Diego: Academic Press. xx, 1398 p.

26. Florencio-Silva, R., et al., *Biology of Bone Tissue: Structure, Function, and Factors That Influence Bone Cells.* Biomed Research International, 2015.

27. Clarke, B., *Normal Bone Anatomy and Physiology.* Clinical Journal of the American Society of Nephrology, 2008. **3**: p. S131-S139.

28. Yin, T. and L. Li, *The stem cell niches in bone.* J Clin Invest, 2006. **116**(5): p. 1195-201.

29. Sims, N.A. and C. Vrahnas, *Regulation of cortical and trabecular bone mass by communication between osteoblasts, osteocytes and osteoclasts.* Arch Biochem Biophys, 2014. **561**: p. 22-8.

30. Robling, A.G., A.B. Castillo, and C.H. Turner, *Biomechanical and molecular regulation of bone remodeling.* Annu Rev Biomed Eng, 2006. **8**: p. 455-98.

31. Andersen, T.L., et al., *A physical mechanism for coupling bone resorption and formation in adult human bone.* Am J Pathol, 2009. **174**(1): p. 239-47.

32. Kong, Y.Y., et al., *OPGL is a key regulator of osteoclastogenesis, lymphocyte development and lymph-node organogenesis.* Nature, 1999. **397**(6717): p. 315-23.

33. Sims, N.A. and T.J. Martin, *Coupling the activities of bone formation and resorption: a multitude of signals within the basic multicellular unit.* Bonekey Rep, 2014. **3**: p. 481.

34. Shafiee, A., et al., *Fetal Bone Marrow-Derived Mesenchymal Stem/Stromal Cells Enhance Humanization and Bone Formation of BMP7 Loaded Scaffolds.* Biotechnol J, 2017. **12**(12).

35. Noble, B.S., et al., *Mechanical loading: biphasic osteocyte survival and targeting of osteoclasts for bone destruction in rat cortical bone.* Am J Physiol Cell Physiol, 2003. **284**(4): p. C934-43.

36. Chow, J.W., et al., *Mechanical loading stimulates bone formation by reactivation of bone lining cells in 13-week-old rats.* J Bone Miner Res, 1998. **13**(11): p. 1760-7.

37. Pittenger, M.F., et al., *Multilineage potential of adult human mesenchymal stem cells.* Science, 1999. **284**(5411): p. 143-7.

38. Caplan, A.I., *Mesenchymal stem cells.* J Orthop Res, 1991. **9**(5): p. 641-50.

39. Dominici, M., et al., *Minimal criteria for defining multipotent mesenchymal stromal cells. The International Society for Cellular Therapy position statement.* Cytotherapy, 2006. **8**(4): p. 315-7.

40. Baker, N., L.B. Boyette, and R.S. Tuan, *Characterization of bone marrow-derived mesenchymal stem cells in aging.* Bone, 2015. **70**: p. 37-47.

41. Furuta, T., et al., *Mesenchymal Stem Cell-Derived Exosomes Promote Fracture Healing in a Mouse Model.* Stem Cells Transl Med, 2016. **5**(12): p. 1620-1630.

42. Petrie Aronin, C.E. and R.S. Tuan, *Therapeutic potential of the immunomodulatory activities of adult mesenchymal stem cells.* Birth Defects Res C Embryo Today, 2010. **90**(1): p. 67-74.

43. Landis, W.J., *The strength of a calcified tissue depends in part on the molecular structure and organization of its constituent mineral crystals in their organic matrix.* Bone, 1995. **16**(5): p. 533-44.

44. Rauh, J., et al., *Bioreactor systems for bone tissue engineering.* Tissue Eng Part B Rev, 2011. **17**(4): p. 263-80.

45. Salter, E., et al., *Bone tissue engineering bioreactors: a role in the clinic?* Tissue Eng Part B Rev, 2012. **18**(1): p. 62-75.

46. Chen, H.C. and Y.C. Hu, *Bioreactors for tissue engineering.* Biotechnol Lett, 2006. **28**(18): p. 1415-23.

47. Yeatts, A.B. and J.P. Fisher, *Bone tissue engineering bioreactors: dynamic culture and the influence of shear stress.* Bone, 2011. **48**(2): p. 171-81.

48. Gaspar, D.A., V. Gomide, and F.J. Monteiro, *The role of perfusion bioreactors in bone tissue engineering.* Biomatter, 2012. **2**(4): p. 167-75.

49. Bancroft, G.N., V.I. Sikavitsas, and A.G. Mikos, *Design of a flow perfusion bioreactor system for bone tissue-engineering applications.* Tissue Eng, 2003. **9**(3): p. 549-54.

50. Kasper, F.K., et al., *Flow perfusion culture of mesenchymal stem cells for bone tissue engineering*, in *StemBook*. 2008: Cambridge (MA).

51. Gharravi, A.M., M. Orazizadeh, and M. Hashemitabar, *Fluid-induced low shear stress improves cartilage like tissue fabrication by encapsulating chondrocytes.* Cell Tissue Bank, 2016. **17**(1): p. 117-22.

52. Li, D., et al., *Effects of flow shear stress and mass transport on the construction of a large-scale tissue-engineered bone in a perfusion bioreactor.* Tissue Eng Part A, 2009. **15**(10): p. 2773-83.

53. Goldstein, A.S., et al., *Effect of convection on osteoblastic cell growth and function in biodegradable polymer foam scaffolds.* Biomaterials, 2001. **22**(11): p. 1279-88.

54. Mauney, J.R., et al., *Mechanical stimulation promotes osteogenic differentiation of human bone marrow stromal cells on 3-D partially demineralized bone scaffolds in vitro.* Calcif Tissue Int, 2004. **74**(5): p. 458-68.

55. Bacabac, R.G., et al., *Nitric oxide production by bone cells is fluid shear stress rate dependent.* Biochem Biophys Res Commun, 2004. **315**(4): p. 823-9.

56. Bancroft, G.N., et al., *Fluid flow increases mineralized matrix deposition in 3D perfusion culture of marrow stromal osteoblasts in a dose-dependent manner.* Proc Natl Acad Sci U S A, 2002. **99**(20): p. 12600-5.

57. Zhao, F., et al., *Flow rates in perfusion bioreactors to maximise mineralisation in bone tissue engineering in vitro.* J Biomech, 2018. **79**: p. 232-237.

58. Holzapfel, B.M., M. Rudert, and D.W. Hutmacher, *[Scaffold-based Bone Tissue Engineering].* Orthopade, 2017. **46**(8): p. 701-710.

59. Burg, K.J., S. Porter, and J.F. Kellam, *Biomaterial developments for bone tissue engineering.* Biomaterials, 2000. **21**(23): p. 2347-59.

60. Yuan, B., S.Y. Zhou, and X.S. Chen, *Rapid prototyping technology and its application in bone tissue engineering.* J Zhejiang Univ Sci B, 2017. **18**(4): p. 303-315.

61. Hao, Z., et al., *The scaffold microenvironment for stem cell based bone tissue engineering.* Biomater Sci, 2017. **5**(8): p. 1382-1392.

62. Arora, S., et al., *Oxygen uptake rate as a tool for on-line estimation of cell biomass and bed temperature in a novel solid-state fermentation bioreactor.* Bioprocess Biosyst Eng, 2018. **41**(7): p. 917-929.

63. Santoro, R., et al., *On-line monitoring of oxygen as a non-destructive method to quantify cells in engineered 3D tissue constructs.* J Tissue Eng Regen Med, 2012. **6**(9): p. 696-701.

64. Simmons, A.D., et al., *Sensing metabolites for the monitoring of tissue engineered construct cellularity in perfusion bioreactors.* Biosens Bioelectron, 2017. **90**: p. 443-449.

65. Simmons, A.D. and V.I. Sikavitsas, *Monitoring Bone Tissue Engineered (BTE) Constructs Based on the Shifting Metabolism of Differentiating Stem Cells.* Ann Biomed Eng, 2018. **46**(1): p. 37-47.

66. Super, A., et al., *Real-time monitoring of specific oxygen uptake rates of embryonic stem cells in a microfluidic cell culture device.* Biotechnol J, 2016. **11**(9): p. 1179-89.

67. Janssen, F.W., et al., *Online measurement of oxygen consumption by goat bone marrow stromal cells in a combined cell-seeding and proliferation perfusion bioreactor.* J Biomed Mater Res A, 2006. **79**(2): p. 338-48.

68. Mishra, A. and B. Starly, *Real time in vitro measurement of oxygen uptake rates for HEPG2 liver cells encapsulated in alginate matrices.* Microfluidics and Nanofluidics, 2009. **6**(3): p. 373-381.

69. Deshpande, R.R. and E. Heinzle, *On-line oxygen uptake rate and culture viability measurement of animal cell culture using microplates with integrated oxygen sensors.* Biotechnol Lett, 2004. **26**(9): p. 763-7.

70. Wang, L., et al., *Spatially monitoring oxygen level in 3D microfabricated cell culture systems using optical oxygen sensing beads.* Lab Chip, 2013. **13**(8): p. 1586-92.

71. Kellner, K., et al., *Determination of oxygen gradients in engineered tissue using a fluorescent sensor.* Biotechnol Bioeng, 2002. **80**(1): p. 73-83.

72. White, S.F., et al., *On-line monitoring of glucose, glutamate and glutamine during mammalian cell cultivations.* Biosens Bioelectron, 1995. **10**(6-7): p. 543-51.

73. White, S.F., et al., *Investigations of Platinized and Rhodinized Carbon Electrodes for Use in Glucose Sensors.* Electroanalysis, 1994. **6**(8): p. 625-632.

74. Pasic, A., et al., *Fiber-optic flow-through sensor for online monitoring of glucose.* Anal Bioanal Chem, 2006. **386**(5): p. 1293-302.

75. Meuwly, F., et al., *Use of glucose consumption rate (GCR) as a tool to monitor and control animal cell production processes in packed-bed bioreactors.* Journal of Biotechnology, 2006. **122**(1): p. 122-129.

76. Sonnaert, M., et al., *Quantitative Validation of the Presto Blue Metabolic Assay for Online Monitoring of Cell Proliferation in a 3D Perfusion Bioreactor System.* Tissue Eng Part C Methods, 2015. **21**(6): p. 519-29.

77. Gloeckner, H., T. Jonuleit, and H.D. Lemke, *Monitoring of cell viability and cell growth in a hollow-fiber bioreactor by use of the dye Alamar Blue.* J Immunol Methods, 2001. **252**(1-2): p. 131-8.

78. Rampersad, S.N., *Multiple applications of Alamar Blue as an indicator of metabolic function and cellular health in cell viability bioassays.* Sensors (Basel), 2012. **12**(9): p. 12347-60.

79. Mueller, D., et al., *Real-time in situ viability assessment in a 3D bioreactor with liver cells using resazurin assay.* Cytotechnology, 2013. **65**(2): p. 297-305.

80. Zhou, X.H., et al., *Noninvasive Real-Time Monitoring by AlamarBlue (R) During In Vitro Culture of Three-Dimensional Tissue-Engineered Bone Constructs.* Tissue Engineering Part C-Methods, 2013. **19**(9): p. 720-729.

81. Uzarski, J.S., et al., *Essential design considerations for the resazurin reduction assay to noninvasively quantify cell expansion within perfused extracellular matrix scaffolds.* Biomaterials, 2017. **129**: p. 163-175.

82. Quent, V.M., et al., *Discrepancies between metabolic activity and DNA content as tool to assess cell proliferation in cancer research.* J Cell Mol Med, 2010. **14**(4): p. 1003-13.

83. Bagnaninchi, P.O., et al., *Towards on-line monitoring of cell growth in microporous scaffolds: Utilization and interpretation of complex permittivity measurements.* Biotechnol Bioeng, 2003. **84**(3): p. 343-50.

84. Bagnaninchi, P.O., et al., *Complex permittivity measurement as a new noninvasive tool for monitoring in vitro tissue engineering and cell signature through the detection of cell proliferation, differentiation, and pretissue formation.* IEEE Trans Nanobioscience, 2004. **3**(4): p. 243-50.

85. Lewis, M.C., et al., *Heterogeneous proliferation within engineered cartilaginous tissue: the role of oxygen tension.* Biotechnol Bioeng, 2005. **91**(5): p. 607-15.

86. Pattappa, G., et al., *The metabolism of human mesenchymal stem cells during proliferation and differentiation.* J Cell Physiol, 2011. **226**(10): p. 2562-70.

87. Grayson, W.L., et al., *Effects of hypoxia on human mesenchymal stem cell expansion and plasticity in 3D constructs.* Journal of Cellular Physiology, 2006. **207**(2): p. 331-339.

88. Guarino, R.D., et al., *Method for determining oxygen consumption rates of static cultures from microplate measurements of pericellular dissolved oxygen concentration.* Biotechnol Bioeng, 2004. **86**(7): p. 775-87.

89. Curcio, E., et al., *Kinetics of oxygen uptake by cells potentially used in a tissue engineered trachea.* Biomaterials, 2014. **35**(25): p. 6829-37.

90. Chen, C.T., et al., *Coordinated changes of mitochondrial biogenesis and antioxidant enzymes during osteogenic differentiation of human mesenchymal stem cells.* Stem Cells, 2008. **26**(4): p. 960-968.

91. Fan, J., et al., *Glutamine-driven oxidative phosphorylation is a major ATP source in transformed mammalian cells in both normoxia and hypoxia.* Molecular Systems Biology, 2013. **9**.

92. Portner, R. and M. Koop, *A model for oxygen supply in fixed bed reactors with immobilized hybridoma cells.* Bioprocess Engineering, 1997. **17**(5): p. 269-275.

93. Wendt, D., et al., *Uniform tissues engineered by seeding and culturing cells in 3D scaffolds under perfusion at defined oxygen tensions.* Biorheology, 2006. **43**(3,4): p. 481-8.

94. VanGordon, S.B., et al., *Effects of Scaffold Architecture on Preosteoblastic Cultures under Continuous Fluid Shear.* Industrial & Engineering Chemistry Research, 2011. **50**(2): p. 620-629.

95. Optics, O. *Oxygen Sensing*. 2018 [cited 2018 Aug. 8].

96. Simmons, A.D., *The Development of a Combined approach for the Real-Time, Non-Destructive Monitoring of In Vitro Bone Tissue Engineered Constructs Utilizing Physio-Metabolic Markers*, in *School of Chemical, Biological, and Materials Engineering*. 2016, University of Oklahoma. p. 120.

97. Fogler, H.S., *Elements of chemical reaction engineering*. Fifth edition. ed. 2016, Boston: Prentice Hall. xxxiii, 957 pages.

98. Cao, C. *Fluid Flow in Packed Beds* 2015; Available from: https://cao.chem.ufl.edu/wp-content/uploads/sites/22/2015/01/Lecture13-2015.pdf

.

99. Kumar, S. and M. Vaidya, *Hypoxia inhibits mesenchymal stem cell proliferation through HIF1alpha-dependent regulation of P27.* Mol Cell Biochem, 2016. **415**(1-2): p. 29-38.

100. Schop, D., et al., *Expansion of human mesenchymal stromal cells on microcarriers: growth and metabolism.* J Tissue Eng Regen Med, 2010. **4**(2): p. 131-40.

101. Levenspiel, O., *Chemical reaction engineering.* Industrial & Engineering Chemistry Research, 1999. **38**(11): p. 4140-4143.

Appendix

A1. Supplemental Methodologies

A1.1 Extraction of Rat Mesenchymal Stem Cells

Rat mesenchymal stem cells (rMSC) were used for all experiments conducted. Cells were extracted from the bone marrow of rat femurs and tibias using methods approved by the University of Oklahoma Institutional Animal Care and Use Committee (IACUC). Rats used were 6 week old male Winstar rats weighing approximately 175-199 grams (Envigo; Hsd:Wi).

Following order and delivery, rats were placed in the animal housing facility (Laboratory Animal Resources) for 3 to 4 days to allow for rats to acclimate to new environment. Once the acclimation period was complete, rats were collected and brought back to the lab for cell extraction. Rats were asphyxiated one by one in a CO_2 chamber using approved methods (American Association for Laboratory Animal Science) whereby CO_2 was added to the chamber at 10% the total chamber volume per minute. Following asphyxiation, all CO_2 was expelled from the chamber before the next rat was introduced to the asphyxiation chamber. Immediately following the death of the rat, the lower half of the rat (hips down to rear feet) was shaved, and then the rat was submerged in 95% ethanol for 5 minutes. The rat was then removed from the ethanol and placed onto the surgical area. A surgical pad was utilized to isolate the desired leg, by forming a small hole in the center of the pad and placing the leg through it. Triodine™ was rubbed on entirety of leg to further sterilize the incision site.

A long incision was first made on the lateral side of the leg from hip to the ankle. First, muscle and connective tissues were cut away from the femur, and the ligament at the hip was cut to allow the femur head to be removed. Muscle and connective tissues were then cut away from tibia, and the ankle joint was severed to allow full removal of the femur and tibia. The knee was

severed at the distal end of the femur and the proximal end of the tibia. The two bones were then placed in bone media. Bone media is comprised of normal αMEM without any FBS supplementation. The same process was completed for the other leg.

The bones, bone media, sterile bone cutters, and sterile forceps were placed in the biological hood. Additionally, αMEM supplemented with 10% FBS was warmed to 37 °C and placed under the hood. 3 mL syringes (BD 3mL Syringe; 309657) and 20 gauge filter needles (Braun; FN-5120) were filled with media, and set to the side until bones were prepared. Two syringes were prepared for each bone. One by one, bones were removed from the bone media. Femurs were cut at the proximal end with bone cutters, and needles were inserted approximately 1 cm into the distal end, and media was flushed through the bone, carrying the bone marrow into a sterile 15 mL falcon tube (Corning; 352196). Tibias were cut at the distal end, and needles were inserted approximately 1 cm into the proximal end of the bone. Again, bone marrow was flushed from the bone using media. The bones from each leg were kept separate from other legs, as was the bone marrow. The bone marrow was then broken up and suspended in same media used to flush bones, and split evenly between 5 cell culture flasks (Corning; 430641U). Each flask was supplemented with αMEM to a final volume of 10 mL. Flasks were then placed into the incubator set to 37°C, approximately 95% humidity, and 5% CO_2 for 4 days. Flasks were then gently rinsed with PBS, and 10 mL of αMEM was added to each flask. Mesenchymal stem cells at this step were considered Passage Zero. Cells were fed every other day from that point on, and ultimately passaged or stored cryogenically once reaching 80% confluency.

A1.2 Cryogenic Storage of Cells

Mesenchymal stem cells used in the experiments were occasionally frozen cryogenically for storage. Cryogenic media was first prepared. Cryogenic media is composed of 90% FBS (Atlanta Biologicals; S11150; Lot K13149) and 10% dimethyl sulfoxide (DMSO) (Sigma-Aldrich; 472301-2.5L). Cells growing in culture flask (Corning; 430641U) were rinsed with 5 mL PBS. Once rinsed, 1 mL trypsin (Sigma-Aldrich; T4049-100ML) was added to the flask, and incubated for 6 minutes (37 °C, 5% CO_2, 95% humidity) to lift the cells. Cells were then rinsed from the flask using 9 mL αMEM and placed in a 15 mL falcon tube (Corning; 362196). The cells were well mixed, and a small sample of approximately 0.2 mL was taken to count cells using a hemocytometer (Bright-Line; 1492). The remaining cells were centrifuged at 1100 rpm for 5 minutes, creating a cell pellet. Media was carefully removed using a vacuum line, and the cell pellet was redistributed in cryogenic media at a concentration of approximately 1 million cells per mL. The cell/cryogenic media solution was pipetted into cryogenic vials (1 mL each), and the vials were placed in Mr. Freeze (Nalgene; 5100-0001) and placed in a -80 °C freezer for 12-24 hours. The vials were then transferred to liquid nitrogen cryogenic storage.

Cells were plated from cryogenic storage by first removing the cells from liquid nitrogen and thawing. The cells and cryogenic media was then pipetted into a cell culture flask, and supplemented with 10 mL αMEM. The following day, all media was pulled off and 10 mL fresh media was added to each cell culture flask. From that point on, media was changed every other day and normal cell passaging occurred.

A1.3 Oxygen Sensor Production

Oxygen sensing modules located at the exit of each bioreactor cassette were designed to allow for accurate measurement of oxygen concentration in the media leaving the bioreactor body. To do so, they were comprised of tubing impermeable to oxygen, a glass housing for the RedEye^{TM} oxygen sensing patch, and an outer cover to mitigate signal loss due to ambient light. The design of the current sensors used were based on OxyMods originally produced by Simmons [96]. Design modifications were completed to correct for issues encountered with first generation model.

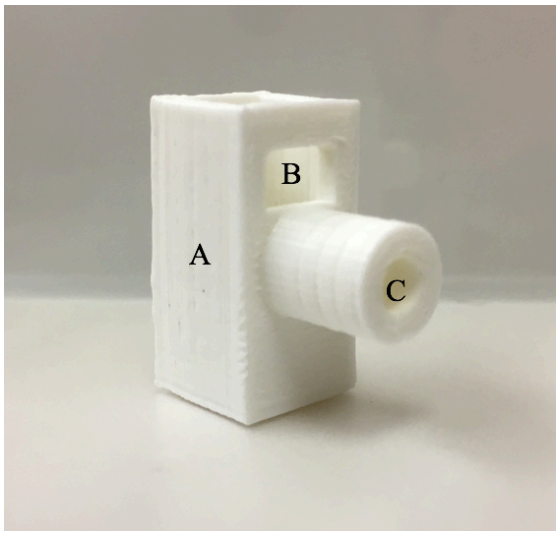

Figure 12: Oxygen Sensing Module Cover
The oxygen sensing module cover has three main features that aid in oxygen concentration measurements: (A) the white plastic used aids in reducing background noise, (B) viewing window to check for air in reactor line, and (C) a cylindrical guide for the probe used in oxygen measurments.

The outer cover seen in **Figure 12** was designed in SolidWorks, and provides 3 main benefits. First, the cover itself is 3D printed from white material. Original OxyMods used white tape around the perimeter of the sensor to aid in sensor readings, so the cover helps level out oxygen readings by providing a solid white background while also blocking ambient light in

room. Second, the cover has a small opening at the top which provides a viewing window to check for air in the sensor. As air will affect the readings, checking for air in the sensor is an important step before measuring oxygen levels in media. Last, the cover has a cylinder that serves as a guide for the probe connected to the NeoFox Viewing System™. The location a reading is taken on the oxygen sensing patches greatly affects the measurement output, so a guide ensures consistent readings are taken.

The inner portion of the sensor was comprised of square tubing (FD #175494) cut into lengths of approximately 1 inch. The oxygen sensing material (Ocean Optics; RE-FOS-4-KIT) was placed in the center of a single side, and the outer cover was slid over the glass tubing, ensuring the probe guide was lined up with the RedEye™ patch. Water proof epoxy was then used to glue two 1/8 inch barbed fittings to the entrance and exit of the sensor, while also gluing the cover over the glass tubing. **Figure 12** shows what the assembly looks like without the cover or the oxygen sensing patch.

Figure 13: Inner Oxygen Sensing Module Chamber
The entrance and exit of the glass tubing have barbed tubing connectors to allow for easy attachment to the exit of the bioreactor system.

A1.4 Oxygen Sensor Calibration

Prior to running the bioreactor systems, all oxygen sensors were calibrated to 0% saturated and 100% saturated oxygen conditions within the bioreactor system. 100% saturation calibrations were completed by constructing the bioreactor system, filling it with DI water in place of media, and placing it in the incubator to reach equilibrium temperature and dissolved oxygen. After media circulated through the reactor system for 12 hours, the sensors were read using the NeoFox Viewing System™ probe, where values for Tau were collected as a reading outputted by the program. Each of these values were recorded as 100% oxygen values. To read 0% oxygen values, a comparable system was setup. A single reservoir was utilized, where a diffusing stone was placed in the DI water to disperse nitrogen gas. Once the water was saturated with nitrogen, it was pumped through the oxygen sensor through oxygen impermeable tubing. This tubing was adjusted to be as short as possible. After allowing 4 hours to reach equilibrium at room temperature, a reading for Tau was taken. Since it was difficult to set up the 0% oxygen system in the incubator, it was found that room temperature produced comparable results. These two values of Tau were used in the two-point calibration on the NeoFox Viewing System™ for oxygen measurements during the bioreactor run.

A1.5 Oxygen Data Collection

The entire bioreactor system shown in **Figure 13** shows the typical organization of the bioreactor system used for flow perfusion tissue engineering. Each of these individual components is connected by oxygen permeable tubing. This allows for complete restoration of oxygenation of media prior to media reentering the bioreactor body. The peristaltic pump provides control over flow rate of media to tissue engineered constructs located in the bioreactor

body, and the reservoir ensures sufficient media is present for supplementation of oxygen, glucose, and other necessary nutrients.

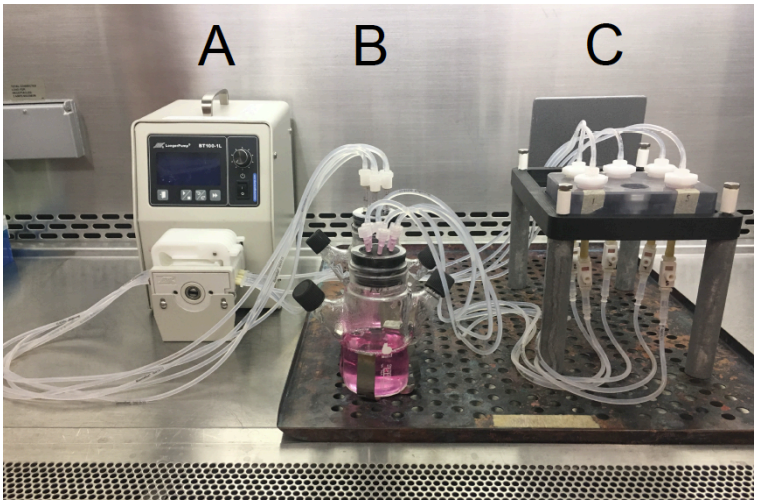

Figure 14: Bioreactor System
The bioreactor system shown consists of (A) peristaltic pump, (B) reservoir system, and (C) the bioreactor body.

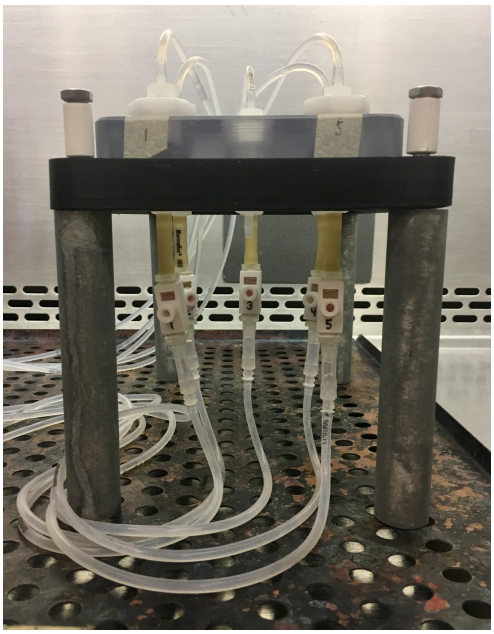

Figure 15: Bioreactor Body
The bioreactor body is the central component to the bioreactor system, where the tissue engineered construct is stored and monitoring components are attached.

The bioreactor body is comprised of multiple parts. The inlet to the tissue engineered construct is located at the top of the body. Media then flows down into the cassette where the construct is housed. Media perfuses through the construct, where oxygen is used by the cells. At the exit of the body is the oxygen sensor. This sensor relies on a patch containing ruthenium and Pt-porphyrin, florescent molecules that have altered properties in the presence of oxygen.

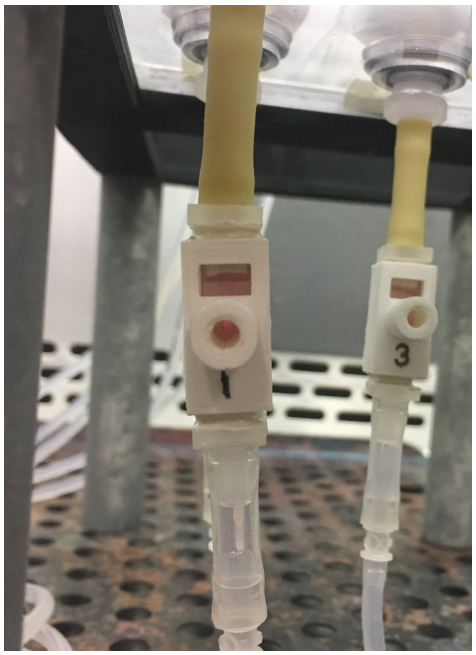

Figure 16: Oxygen Sensing Module
Oxygen sensing modules are located at the immediate exit of the reactor system, providing accurate measurement of oxygen levels in media leaving construct.

After exiting the bioreactor, the media flows through a small section of yellow tubing that has low gas permeability (See **Figure 15**). This tubing ensures that the oxygen concentration at the exit of the construct is the same as what is read by the oxygen sensor. The media then flows into the body of oxygen sensor, a housing that contains an internal glass tube surrounded by a 3D printed holder. This 3D printed object provides a solid white background (something that increases precision of oxygen measurements) and also gives a guide for the probe used to measure oxygen. The circle seen in the center of the housing is the guide, with the center open to

allow access to the oxygen patch. This oxygen sensing patch is located inside the glass tubing, where it can come in direct contact with the media exiting the bioreactor body. The small opening above the probe guide is used as an indicator for air that has leaked into the system. In the presence of air, the sensor no longer functions for media oxygen concentration measurements.

Figure 17: Oxygen Sensing Probe
The probe used to read the oxygen concentration is placed into the oxygen sensing module, and relays information to the NeoFox Viewing System™ for analysis.

To read the oxygen concentration, a fiber optic probe seen in **Figure 16** is placed against the glass directly in front of the oxygen sensing patch. This probe emits a blue light (450 nm). In the presence of blue light and oxygen, the patch emits florescence at visible wavelengths. This florescence is collected by and sent back through the same probe for detection by an avalanche photodiode. This reading for florescence intensity is measured relative to the initial emission of the blue light. It is then correlated to an oxygen concentration using the Stern-Volmer equation. Each oxygen sensor is calibrated prior to each use. It is important to calibrate the sensors, as their properties gradually change over time.

A2. Residence Time Distribution Analysis

A2.1 System Design and Preparation

To collect data for the residence time distribution analysis, the bioreactor system had to be set up to allow for dye data collection. Initially, the scaffold disks were purged of air using the technique outlined in **Section 2.2.** DI water was pumped through the cassette, purging the system of any air. The scaffold disks were placed into the cassette, and DI water was again pumped through the cassette and scaffold, purging the system of any residual air. Entrance and Exit are labeled in **Figure 18.** Once all air was removed, the Exit was clamped, and the DI line to the entrance was disconnected from the Entrance. The line from the dye reservoir was connected to the Entrance, and the clamp was removed from the Exit. Dye solution was pumped through the scaffold, in line with arrows shown in **Figure 18,** at the desired flow rate. Effluent was collected at the Exit, and was analyzed for dye composition.

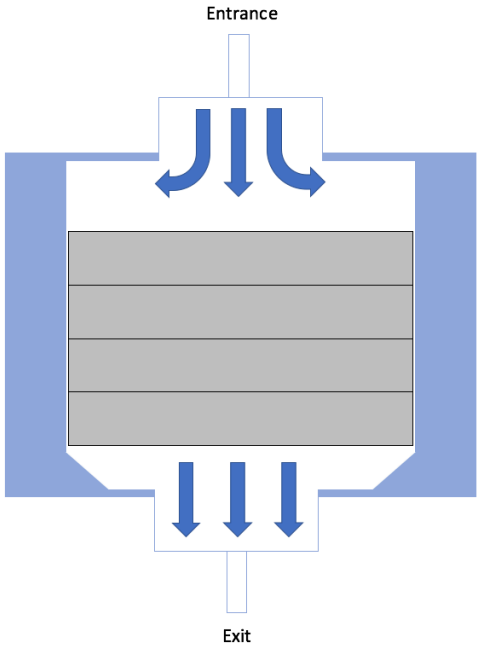

Figure 18: Cassette Cross-sectional View
Cross-sectional view of the cassette holding 4 scaffold disk layers. Arrows indicate the direction of flow through the cassette. Entrance and exit to the cassette are labeled, and are referred to as such.

A2.2 Residence Time Analysis Functions

The cumulative distribution function, F(t), is indicative of the amount of time a particular molecule of fluid has spent in the bioreactor. This function is plotted against time, showing the fraction of molecules that has spent that amount of time (t) or less in the bioreactor [97]. For example, if F(1000) = 0.85, it would mean that 85% of the molecules exiting at t=1000 seconds have spent no more than 1000 seconds in the bioreactor system. **Figure 19** shows example plots of the cumulative distribution function relative to time in seconds for each flow rate tested. From these graphs, it can be deduced that as flow rate increases, the less time it takes to reach a F(t) value of 1.

The residence time distribution function, E(t), is also used to describe how long particular molecules spent in the reactor, where the derivative of E(t) can be used to determine the mean residence time [97]. This function shows what portion of molecules likely spent the associated time, t, in the reactor system. **Figure 20** shows an example of the plot of E(t) with respect to time in seconds for each flow rate tested.

The normalized residence time distribution function, E(θ), gives an indication of the residence time distribution function so that it can be compared to reactors of different sizes. **Figure 21** shows an example plot of E(θ), allowing the derived functions to be compared with literature values for each flow rate tested. **Figure 22** shows a theoretical normalized residence time distribution function plot for laminar flow reactor, which shows similar characteristics to experimentally obtained plots for all flow rates tested. Previous research likened the flow characteristics of these bioreactor systems to plug flow. However, experimentally obtained E(θ) plots do are not comparable to theoretical plug flow graphs, indicating the current bioreactor design is not well approximated by plug flow. **Figure 23** shows what normalized residence time

distribution functions for plug flow would look like with varying amounts of dispersion, none of which have the same characteristic spike and subsequent drop seen in experimental normalized residence time distribution functions.

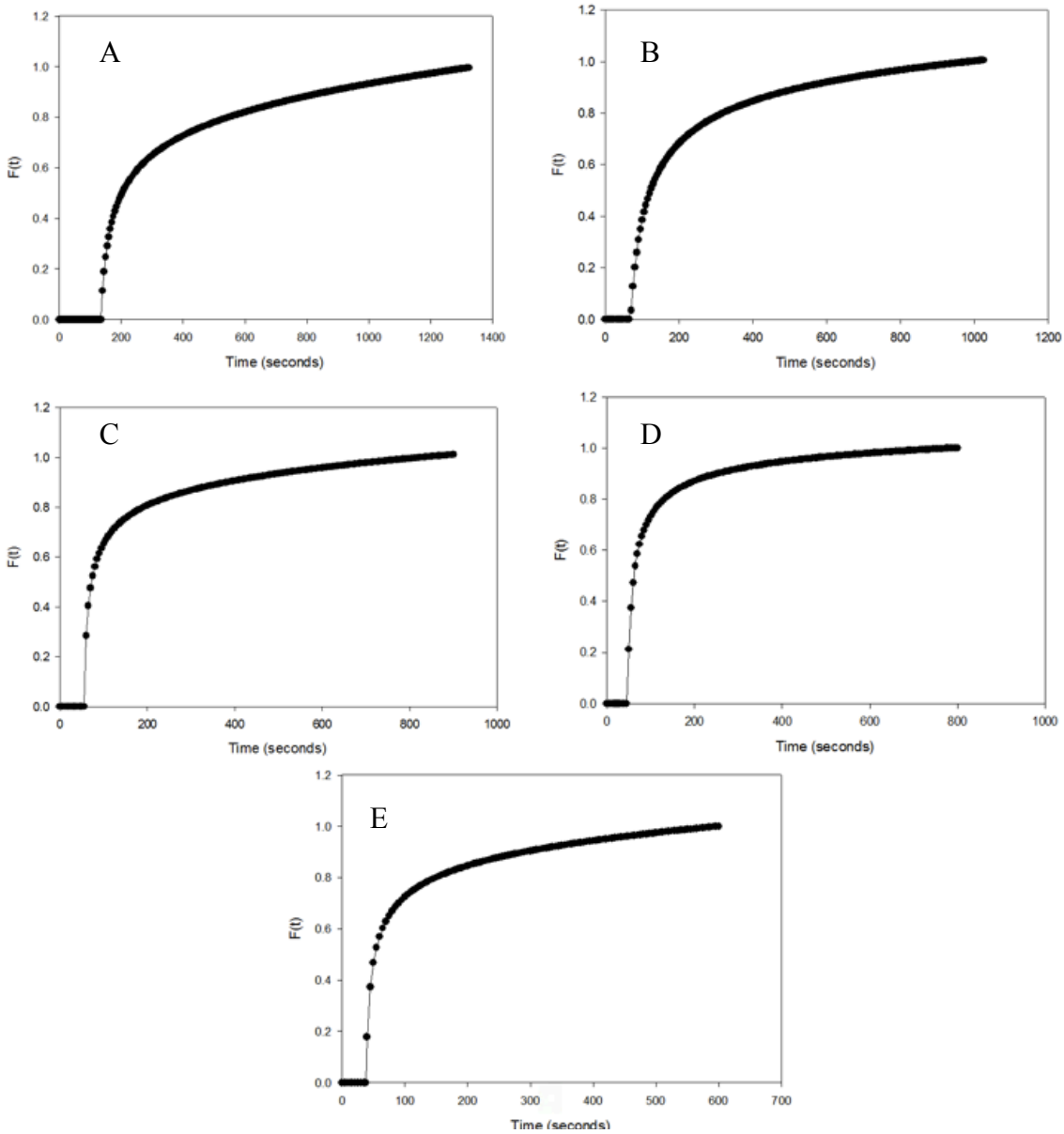

Figure 19: Cumulative Distribution Functions
Example graphs of the cumulative distribution functions, F(t), for each flow rate tested are plotted against time (t) in seconds. These graphs show the approximate time at which all molecules in the reactor at time zero have exited the system. Each graph corresponds to a particular flow rate: (A) 150 µL/min, (B) 300 µL/min, (C) 450 µL/min, (D) 600 µL/min, and (E) 750 µL/min.

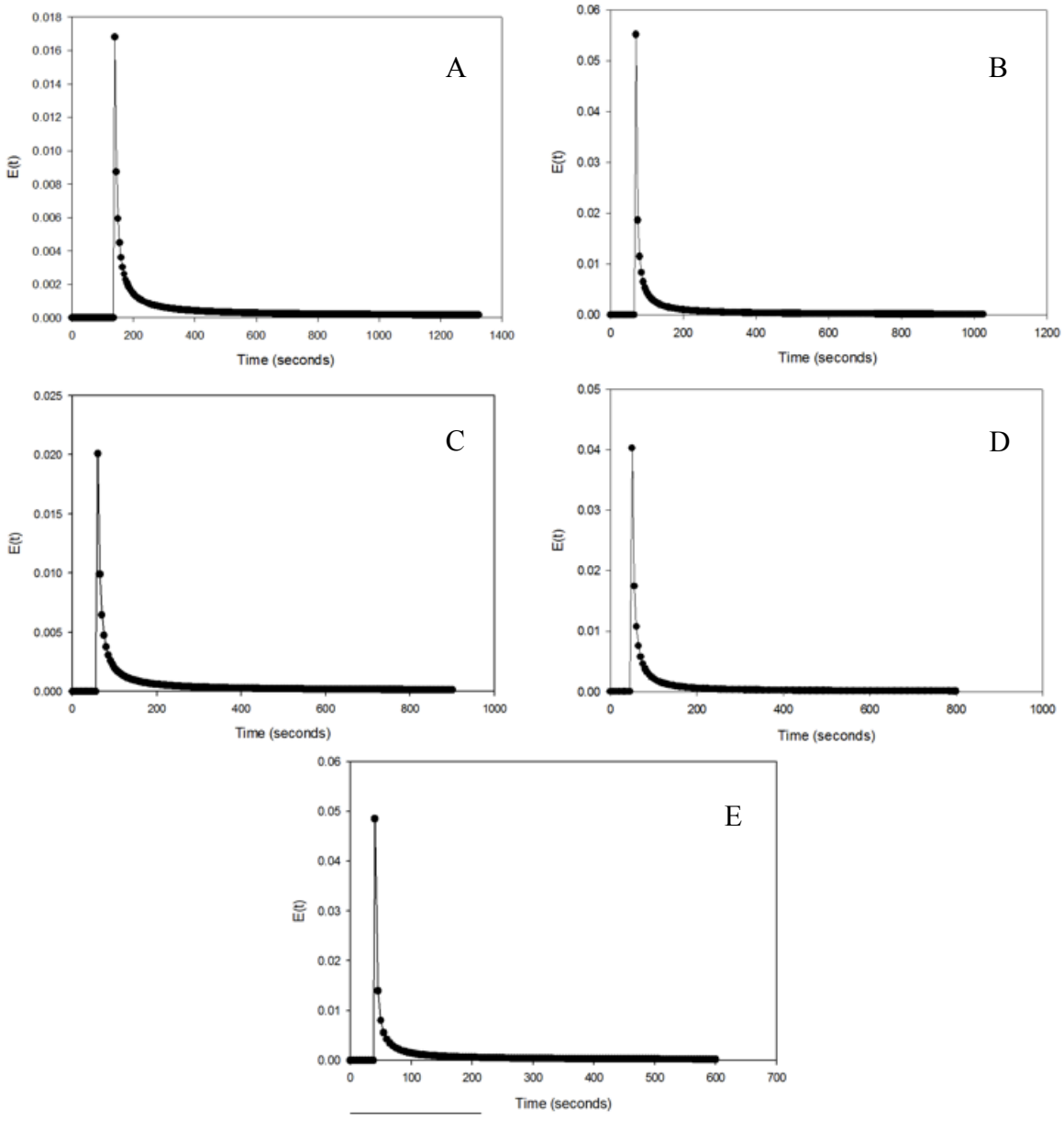

Figure 20: Residence Time Distribution Functions
Example graphs of the residence time distribution functions, E(t), for each flow rate tested are plotted against time (t) in seconds. These graphs show the approximate time at which an amount of molecules in the reactor at time zero have exited the system. Each graph corresponds to a particular flow rate: (A) 150 µL/min, (B) 300 µL/min, (C) 450 µL/min, (D) 600 µL/min, and (E) 750 µL/min.

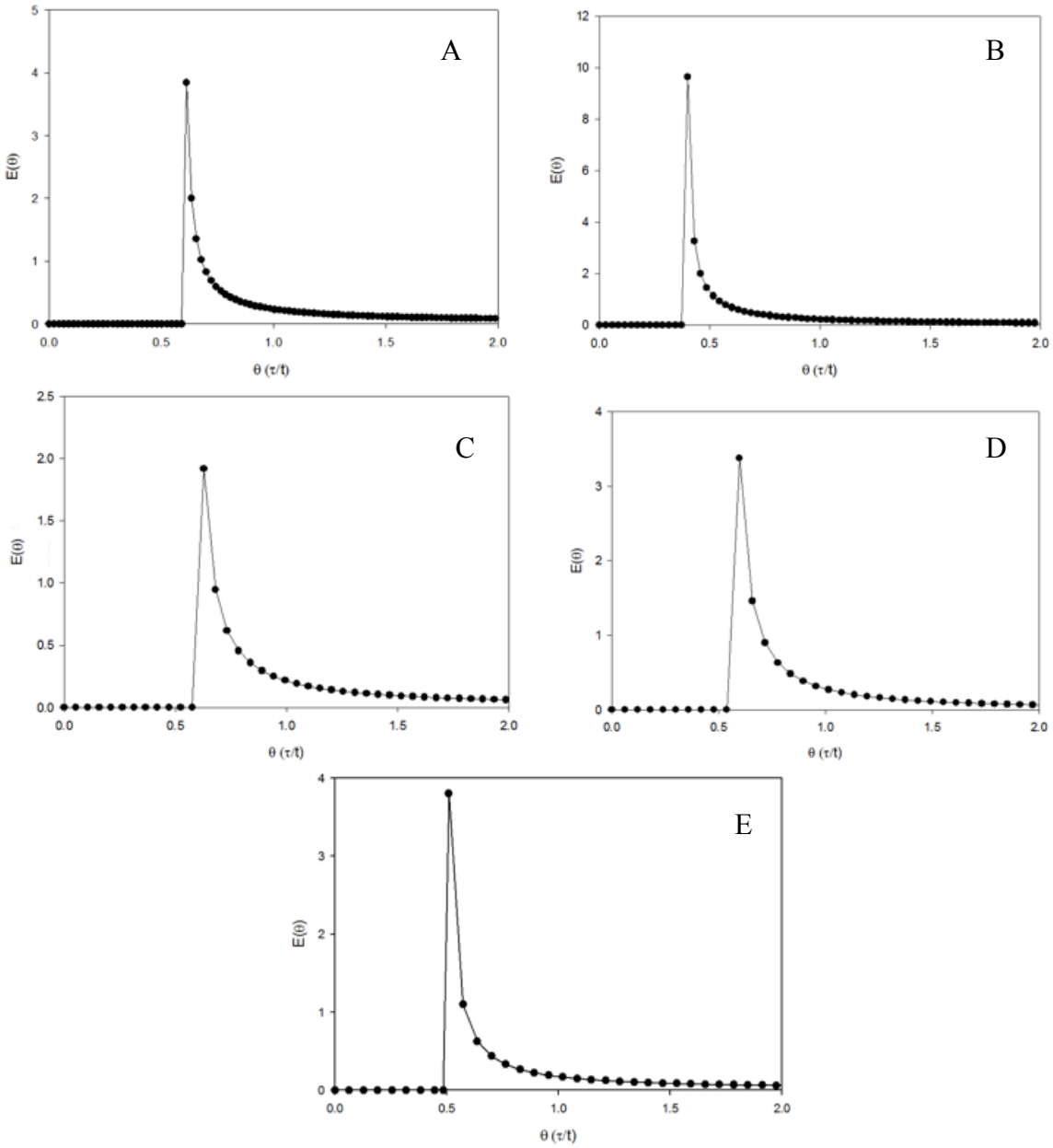

Figure 21: Normalized Residence Time Distribution Functions

Example graphs of the normalized residence time distribution functions, E(θ), for each flow rate tested are plotted against theta (θ). These graphs show the approximate time at which an amount of molecules the reactor at time zero have exited the system, normalized to residence time to allow for comparison to other reactor sizes. Each graph corresponds to a particular flow rate: (A) 150 µL/min, (B) 300 µL/min, (C) 450 µL/min, (D) 600 µL/min, and (E) 750 µL/min.

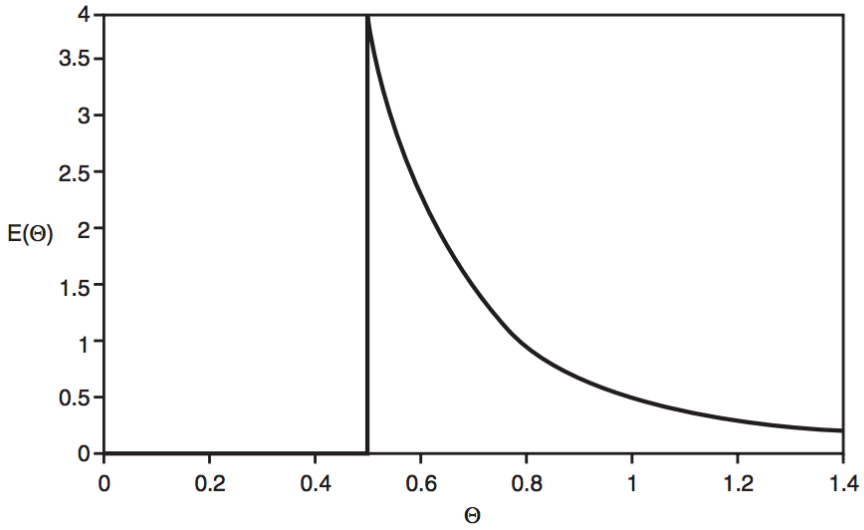

Figure 22: Laminar Flow Theoretical Normalized Residence Time Distribution Function
Theoretical normalized residence time distribution functions, E(θ), for a laminar flow reactor, adapted from Figure 13-9 in Fogler [97]. This graph serves as a comparison to experimentally obtained normalized residence time distribution functions.

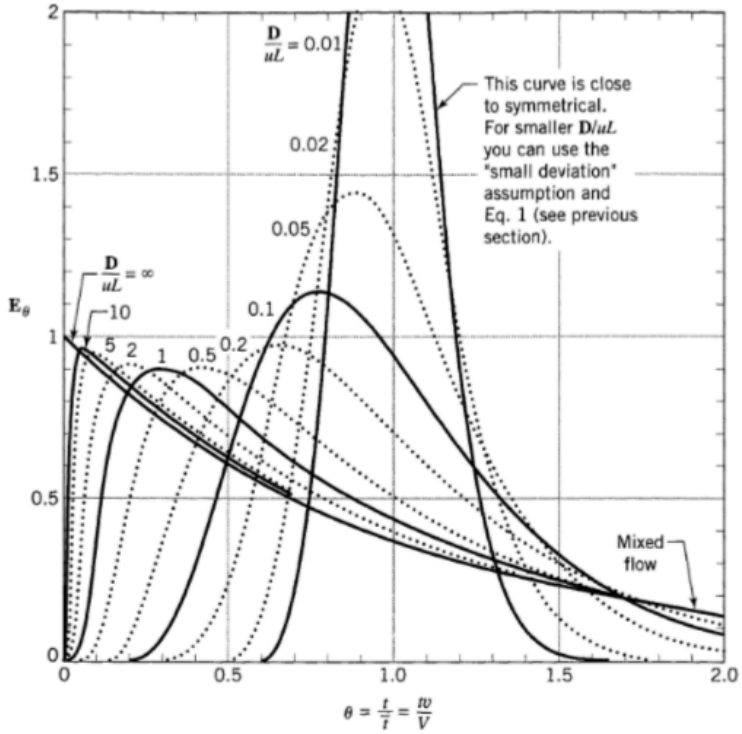

Figure 23: Plug Flow Theoretical Normalized Residence Time Distribution Function
Theoretical normalized residence time distribution functions, E(θ), for a plug flow reactor, adapted from Levenspiel [101]. This graph serves as a comparison to experimentally obtained normalized residence time distribution functions.